

Septins guide noncentrosomal microtubules to promote focal adhesion disassembly in migrating cells

Daniel Merenich^a, Konstantinos Nakos^b, Taylor Pompan^a, Samantha J. Donovan^a, Amrik Gill^a, Pranav Patel^a, Elias T. Spiliotis^b, and Kenneth A. Myers^{a,*}

^aDepartment of Biological Sciences, University of the Sciences in Philadelphia, Philadelphia, PA 19104; ^bDepartment of Biology, Drexel University, Philadelphia, PA 19104

ABSTRACT Endothelial cell migration is critical for vascular angiogenesis and is compromised to facilitate tumor metastasis. The migratory process requires the coordinated assembly and disassembly of focal adhesions (FA), actin, and microtubules (MT). MT dynamics at FAs deliver vesicular cargoes and enhance actomyosin contractility to promote FA turnover and facilitate cell advance. Noncentrosomal (NC) MTs regulate FA dynamics and are sufficient to drive cell polarity, but how NC MTs target FAs to control FA turnover is not understood. Here, we show that Rac1 induces the assembly of FA-proximal septin filaments that promote NC MT growth into FAs and inhibit mitotic centromere-associated kinesin (MCAK)-associated MT disassembly, thereby maintaining intact MT plus ends proximal to FAs. Septin-associated MT rescue is coupled with accumulation of Aurora-A kinase and cytoplasmic linker-associated protein (CLASP) localization to the MT between septin and FAs. In this way, NC MTs are strategically positioned to undergo MCAK- and CLASP-regulated bouts of assembly and disassembly into FAs, thereby regulating FA turnover and cell migration.

Monitoring Editor

Amy Gladfelter
University of North Carolina,
Chapel Hill

Received: Jun 30, 2021

Revised: Feb 7, 2022

Accepted: Mar 4, 2022

INTRODUCTION

Endothelial cell (EC) migration is an essential process for normal vascular development, maintaining tissue homeostasis, and EC angiogenesis is a driving factor for tumor metastasis (Folkman, 1995;

This article was published online ahead of print in MBoC in Press (<http://www.molbiolcell.org/cgi/doi/10.1091/mbc.E21-06-0334>) on March 11, 2022.

The authors declare no competing financial interests.

Author contributions: D.M.: conceptualization, formal analysis, investigation, methodology, project administration, supervision, visualization, writing. K.N.: investigation, writing. T.P.: investigation, visualization. S.J.D.: investigation. A.G.: investigation. P.P.: formal analysis, investigation. E.T.S.: conceptualization, funding acquisition, resources, writing. K.A.M.: conceptualization, funding acquisition, methodology, project administration, resources, supervision, visualization, writing.

*Address correspondence to: Kenneth A. Myers (k.myers@uscience.edu).

Abbreviations used: CAMSAP, calmodulin-regulated spectrin-associated protein; CA-Rac1, constitutively active Rac1; CLASP, cytoplasmic linker-associated protein; DN-Rac1, dominant-negative Rac1; EB, end-binding; EC, endothelial cell; FA, focal adhesion; FL, full length; HUVECs, human umbilical vein endothelial cells; KD, knockdown; MAP, microtubule-associated protein; MCAK, mitotic centromere-associated kinesin; MT, microtubule; NC, noncentrosomal; PA-Rac1, photo-activatable Rac1; γ -TuNA, γ -TuRC-mediated nucleation activator.

© 2022 Merenich et al. This article is distributed by The American Society for Cell Biology under license from the author(s). Two months after publication it is available to the public under an Attribution-NonCommercial-Share Alike 4.0 International Creative Commons License (<http://creativecommons.org/licenses/by-nc-sa/4.0>).

"ASCB®," "The American Society for Cell Biology®," and "Molecular Biology of the Cell®" are registered trademarks of The American Society for Cell Biology.

Risau, 1997; Saariisto et al., 2000). ECs respond to extracellular cues to polarize and undergo continuous morphological adaptations that facilitate movement. Innate to this process is the coordinated assembly and disassembly of focal adhesion (FA) complexes, as well as the dynamic reorganization of the actin and microtubule (MT) network. Studies have shown that in response to integrin engagement of the extracellular matrix (ECM), nascent FAs assemble within the cell's leading edge and undergo a maturation process, which involves the formation of actin stress fibers through which forces are transduced to the ECM and thereby drive polarized and directional cell movement (Kaverina et al., 1999; Miller et al., 2009; Gardel et al., 2010; Parsons et al., 2010; Rooney et al., 2010; Myers et al., 2011).

FA assembly must be coupled with FA disassembly to facilitate cell advance and productive migration. FA disassembly is driven through encounters with the MT cytoskeleton (Krylyshkina et al., 2002; Ridley, 2003; Broussard et al., 2008; Vicente-Manzanares et al., 2009). The spatial and temporal regulation of MT-FA encounters involves a host of proteins that drive FA destabilization and disassembly. Signaling cues that coordinate protein localization and function within FAs are known to be provided by Rho family GTPases. Nascent FA formation is characterized by increased Rac1 activity and reduced RhoA activity, while FA maturation, association

with actin stress fibers, and actomyosin contractility require elevations in RhoA activity (Lawson and Burridge, 2014). Rho family GTPases have dramatic effects on the MT cytoskeleton, including the initiation of signaling cascades that target MT-associated proteins (MAPs) responsible for directly regulating MT dynamic instability. For example, Rac1 activation promotes leading edge MT assembly, initializing a positive feedback loop that drives continued cell polarity (Waterman-Storer and Salmon, 1999; Waterman-Storer et al., 1999; Wittmann et al., 2003), while activation of RhoA and its kinase ROCK is sufficient to initiate MT disassembly (Bhadriraju et al., 2007; Ezratty et al., 2009). MAPs that are activated by Rho GTPases have also been identified to localize within FAs (Wu et al., 2008; Kumar et al., 2009; Matsumoto et al., 2010; Stehbins et al., 2014), suggesting a potential role in linking MT assembly and FA destabilization.

MAPs have been implicated directly in cell polarization and cell migration. Experimental evidence has established a Rac1-Aurora-A kinase signaling pathway that locally inhibits the activity of the MT depolymerizing kinesin, mitotic centromere-associated kinesin (MCAK), to polarize MT growth during EC migration (Braun et al., 2014). MCAK has also been shown to play a role in controlling FA dynamics, as loss of MCAK revealed altered FA assembly and disassembly rates and defects in polarized migration (Moon et al., 2021; Zong et al., 2021). Rac1 has also been shown to inhibit the GSK3 β kinase, resulting in enhanced MT association with cytoplasmic linker-associated protein (CLASP), a MAP that protects MTs from catastrophe, and is known to play a critical role in the regulation of FA stability (Wittmann and Waterman-Storer, 2005; Stehbins et al., 2014). Interestingly, both MCAK and CLASP bind directly to EB1 (Mennella et al., 2005; Mimori-Kiyosue et al., 2005; Lee et al., 2008; Gouveia and Akhmanova, 2010; Marvin et al., 2011; Ashley et al., 2014; Braun et al., 2014; Akhmanova and Casper, 2015; D'Angelo et al., 2017; Myer and Myers, 2017; Aher et al., 2018), placing them at the growing MT plus end, an ideal location to manage interactions between MTs, actin, and FAs.

Recent discoveries have identified that not all MTs are functionally equivalent. In ECs, noncentrosomal (NC) MTs were found to be sufficient to drive cell polarity, sprouting of branched protrusions, and motility, while MTs nucleated at the centrosome were dispensable (Martin et al., 2018). It was also identified in a human embryonic kidney cell line that NC MTs are responsible for controlling FA dynamics when cells are challenged to durotax in response to variable stiffness gradients (Rong et al., 2021). These data indicate that cells can distinguish between centrosomal and NC MTs and raise important questions regarding the molecular mechanism underlying how NC MTs are specifically targeted for assembly into FAs.

Septin GTPases are an integral component of the actin and MT cytoskeleton (Kremer et al., 2005; Mostowy and Cossart, 2012), and septins have been previously shown to promote nascent FA stability and maturation (Dolat et al., 2014). Septins associate with subsets of MTs in the perinuclear cytoplasm, as well as within the cell periphery where they localize proximal to the plasma membrane and FAs (Bowen et al., 2011). Septins are critical for the organization of the actin stress fiber network at peripheral FAs and promote MT plus end growth into membrane protrusions and FAs (Bowen et al., 2011; Dolat et al., 2014; Nölke et al., 2016). How septin localization is controlled and how septins affect MT-FA interactions is not known.

Here, we set out to determine how NC MTs polymerize into FAs and function in EC FA dynamics. Our results show that Rac1 activation drives the spatial positioning of septins adjacent to FAs, where septins redirect NC MT polymerization into FAs. Further, we identify that septins function to stall MCAK-induced disassembly of NC MTs.

In this way, FA-adjacent septins maintain intact NC MT plus ends in close proximity to FAs and promote iterative bouts of MT assembly and disassembly to induce FA disassembly.

RESULTS

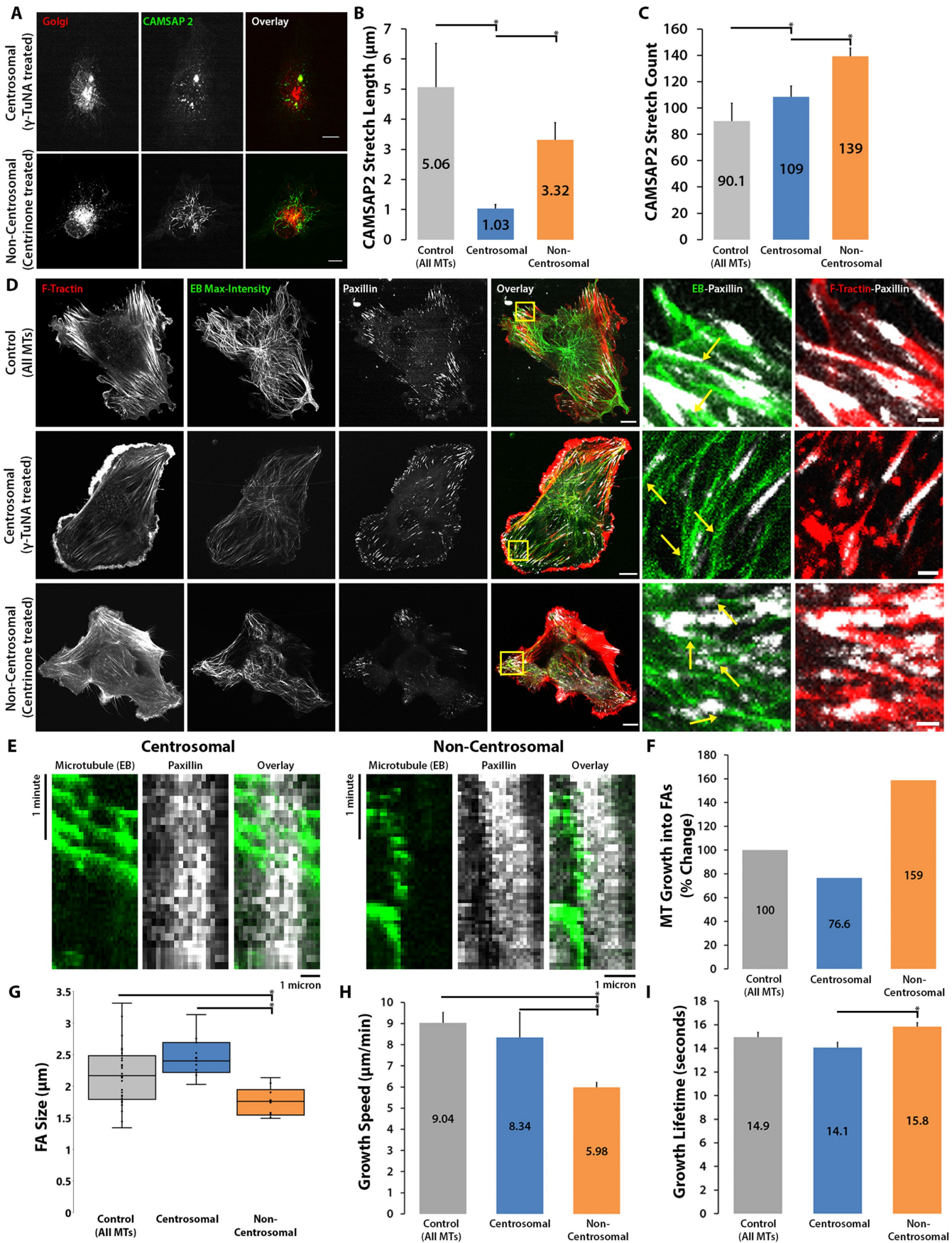
NC MTs polymerize into FAs and reduce FA size

To determine the contribution of centrosomal and NC MTs to FA disassembly in ECs, we expressed GFP-EB3 to label growing MT plus ends and fluorescently tagged paxillin to label FAs. To isolate centrosomal and NC MTs in cells, we used a mutant form of the γ -TuRC-mediated nucleation activator (γ -TuNA), which inhibits the nucleation of NC MTs, resulting in only centrosomally derived MTs (Choi et al., 2010; Sanders et al., 2017; Wu and Akhmanova, 2017), and centrione, which inhibits the nucleation of centrosomal MTs, resulting in only NC MTs (Wong et al., 2015). To confirm that these compounds shift the MT network from centrosomal to NC MTs, and vice versa, we expressed GFP-calmodulin-regulated spectrin-associated protein 2 (CAMSAP2), a specific marker of NC MT minus ends. In the γ -TuNA condition, the CAMSAP2 appeared as mostly diffuse GFP or punctate structures near the cell center (Figure 1A, top row), while in the centrione condition, CAMSAP2 was observed to form short filamentous stretches that were localized adjacent to the Golgi apparatus at the position of NC MT minus ends (Figure 1A, bottom row). Measurements revealed that both the length of GFP-CAMSAP2 labeling of MTs (termed "stretch length"; Figure 1B) and the total number of CAMSAP2 (termed "stretch count"; Figure 1C) were significantly reduced in the γ -TuNA condition. These two groups were compared with a control group that was not treated and therefore maintained the ability to nucleate both centrosomal and NC MTs (termed "All MTs").

Compared with control cells (Figure 1D, top row), visualization of MT organization and dynamics in ECs with centrosomal-only MTs showed that GFP-EB3-labeled MT plus ends grow radially from the centrosome and along actin bundles near FAs but strikingly bypass FAs and terminate at the cell periphery (Figure 1D, middle row). In ECs with NC MTs, however, the majority of EB3 comet tracks originated within peripheral regions of the cell, were typically aligned with actin bundles, and consistently terminated at the position of paxillin-labeled FAs, resulting in accumulation of MT plus ends at FAs (Figure 1D, bottom row). Kymograph analysis of time-lapse movies revealed that NC MTs that tracked to FAs would consistently either stall and disappear within the adhesion or undergo bouts of disassembly and rapid regrowth into FAs, while centrosomal MTs consistently polymerized beyond the FAs (Figure 1E and Supplemental Videos 1 and 2). The number of NC MTs that grew into FAs was 59% and 82% higher than the number of MTs that targeted FAs in control and centrosomal cells, respectively (Figure 1F). In cells with NC-only MTs, FAs were 27.9% smaller than in cells with centrosomal-only MTs (Figure 1G; $p < 0.05$). Measurements of mean MT number in control, centrosomal-only MTs, and NC-only MTs confirmed that the reduction in FA size was not due to increased numbers of MTs present in conditions of NC-only MTs (Supplemental Figure S1, A and B). Measurements of MT assembly dynamics revealed that NC MTs grew significantly slower than centrosomal MTs (5.98 vs. 8.34 $\mu\text{m}/\text{min}$; Figure 1H), while growth lifetimes of NC MTs were significantly longer than those of centrosomal MTs (15.8 vs. 14.1 s; Figure 1I). These data indicate that NC MT plus ends display slow and persistent growth into peripheral FAs and reduce FA size.

Septin directs NC MTs to FAs and regulates FA dynamics

Visual comparison of centrosomal and NC MT growth trajectories revealed that many of the NC MT growth tracks underwent a



change in direction typically within a few microns of peripheral FAs and before terminating within FAs (Figure 2A). As septin GTPases have been previously implicated in MT guidance to membrane protrusions and FAs (Dolat et al., 2014; Nölke et al., 2016), we examined whether septins play a role in MT targeting and polymerization into FAs. We expressed mCherry-Septin 7 (as a proxy for Septin 2,6,7 filaments; see also Supplemental Figure S1, C–I) and performed time-lapse confocal imaging, which revealed that MT ends come in contact with FA-proximal septin filaments before switching to a curvilinear movement into FAs (Figure 2B, Supplemental Figure S2A, and Supplemental Video 3). Quantification of the frequency of MT growth into FAs revealed that 96.5% of MTs that colocalized with peripheral Septin 7 subsequently terminated within paxillin-labeled FAs (Figure 2C). To further determine the contribution of septins to MT growth into FAs, we compared exogenous Septin 7 expression with Septin 7 knockdown (KD). Using small interfering RNA (siRNA), we were able to reduce cellular levels of Septin 7 to 17.2% of endogenous levels (Figure 2D and Supplemental Figure S2, B and C). Comparative analysis of the growth of centrosomal-only and NC MTs into FAs showed that NC MTs were 2.38 times more likely to colocalize with peripheral Septin 7 and were 3.44 times more likely to grow into FAs, while septin KD resulted in reduced NC MT growth into FAs that was similar to that of centrosomal MTs (Figure 2E).

To determine the effects of Septin 7 on MT assembly dynamics, we measured EB3 growth speed and growth lifetime in ECs expressing Septin 7. We first confirmed that Septin 7 expression by itself did not alter whole-cell MT growth speed or lifetime (Supplemental Figure S2, D and E). We next measured MT polymerization dynamics with either centrosomal or NC MTs before and after colocalization with Septin 7 and compared them to MTs that did not colocalize with Septin 7. This revealed that, in both groups of MTs, the speed of polymerization was reduced after colocalization with Septin 7 (i.e., between Septin 7 and the FA; Figure 2F). However, NC MTs tended to move slower than centrosomal and were significantly slower after interacting with septins (Cent = 8.07–6.91 $\mu\text{m}/\text{min}$, NC = 7.44–5.41 $\mu\text{m}/\text{min}$; Figure 2F). NC MTs that did not colocalize with peripheral Septin 7 assembled at rates similar to the “before septin colocalized” measurement (6.84 vs. 7.44 $\mu\text{m}/\text{min}$). In contrast, centrosomal MT growth speeds were statistically similar independent of Septin 7 colocalization, while septin KD increased MT growth speed for both centrosomal and NC MTs (Figure 2F). Analysis of MT growth lifetime revealed similar effects on both centrosomal and NC MTs before and after Septin 7 colocalization, including increased lifetime after Septin 7 colocalization that was reduced to the “before septin colocalized” measurement under conditions of Septin 7 KD. In both centrosomal and NC MT groups, the longest MT growth lifetimes were measured for MTs that by-

passed the septin and polymerized toward the cell membrane (septin not colocalized; Figure 2G). Together, these data support an essential role for peripheral septins in directing NC MT for polymerization into FAs.

To evaluate the effects of septin on FA behaviors, we measured FA size and assembly and disassembly rates under control and septin KD conditions (Figure 2, H–J). Analysis revealed that FA size was significantly reduced in NC MT cells compared with centrosomal MT cells and this effect was reversed upon septin KD in the NC MT group but was not significantly affected in the centrosomal MT group (Figure 2H). To identify the effects of NC MTs and septin on FA dynamics, we measured and compared FA assembly and disassembly rates. Analysis revealed that the rates of both FA assembly and disassembly were significantly increased in cells with NC-only MTs, compared with cells with centrosomal-only MTs (Cent assembly = 0.0184 min^{-1} , Cent disassembly 0.0198 min^{-1} , NC assembly = 0.268 min^{-1} , NC disassembly 0.0265 min^{-1} ; Figure 2I). KD of Septin 7 resulted in significantly reduced FA assembly and disassembly rates (Figure 2J) that were similar to rates measured in centrosomal-only MTs (comparing Figure 2, J and I). These data indicate that Septin 7 is required for increased FA dynamics and reduced FA size in a NC MT-dependent manner.

CLASP regulates septin-associated MT dynamics to control FA size

In epithelial cells, the MT-associated protein CLASP plays a key role in FA capture of MTs and importantly, this function of CLASP is required for cargo trafficking to FAs including matrix metalloproteases that contribute to FA disassembly and remodeling of the ECM (Stehbens et al., 2014). We set out to determine whether septins and FA-associated CLASP might be working together to facilitate MT capture at FAs. Similar to epithelial cells, CLASP localized to both MTs and adjacent to FAs in ECs (Figure 3A). Kymograph analysis of CLASP and Septin 7 revealed that CLASP colocalized with EB3 on growing MT plus ends and that CLASP association with MTs typically occurred after NC MTs had made contact with Septin 7 filaments as they approached FAs (Figure 3B). Notably, septin-associated, CLASP-labeled MTs were observed to assemble into FAs followed by concurrent dissociation of CLASP and disassembly of MTs back to the septin, followed again by CLASP relocation and MT rescue (Figure 3C). Measurements of FA size revealed that CLASP expression resulted in reduced FA size, which is consistent with previous reports (Stehbens et al., 2014). Moreover, this effect of reduced FA size was also observed in ECs with centrosomal-only and NC MTs (Figure 3, D and E).

Previous studies had identified that, unlike CLASP that localizes to the MT lattice or CLASP that associates with EBs on the MT plus end, FA-associated CLASP localized to FAs independent of MT

FIGURE 1: NC MTs polymerize into FAs and reduce FA size. (A) HUVEC expressing mApple-Golgi and GFP-CAMSAP2 showing CAMSAP2 localization in conditions of centrosomal (top row) or NC (bottom row) MTs. (B, C) Quantification of CAMSAP2 stretch length (B) and count (C). (D) HUVECs expressing mCherry-F-Tractin and GFP-EB3 and white paxillin in control (all MTs; top row), centrosomal MT (middle row), and NC MT (bottom row) cells. Yellow boxes in overlay images indicate the zoom regions shown to the right. Zoom regions show MT organization (yellow arrows in green EB max-intensity projections) relative to FAs (white) and actin organization (red) relative to the same FAs (far right panels). (E) Representative kymographs of GFP-EB3 and FA dynamics (paxillin; white) in cells with centrosomal MTs (left) or NC MTs (right; related to Supplemental Video 1 and 2). (F) Quantification of the percent change in EB growth into FAs. (G–I) Comparison of FA size (G), MT growth speed (H), and MT growth lifetime (I) in HUVECs with control, centrosomal, or NC MTs. Error bars show $\pm\text{SD}$ in B and C and $\pm\text{SE}$ in H and I. Scale bars = 10 μm , whole cell view; 1 μm , zoomed view. Student's *t* test; *p* (*) < 0.05.

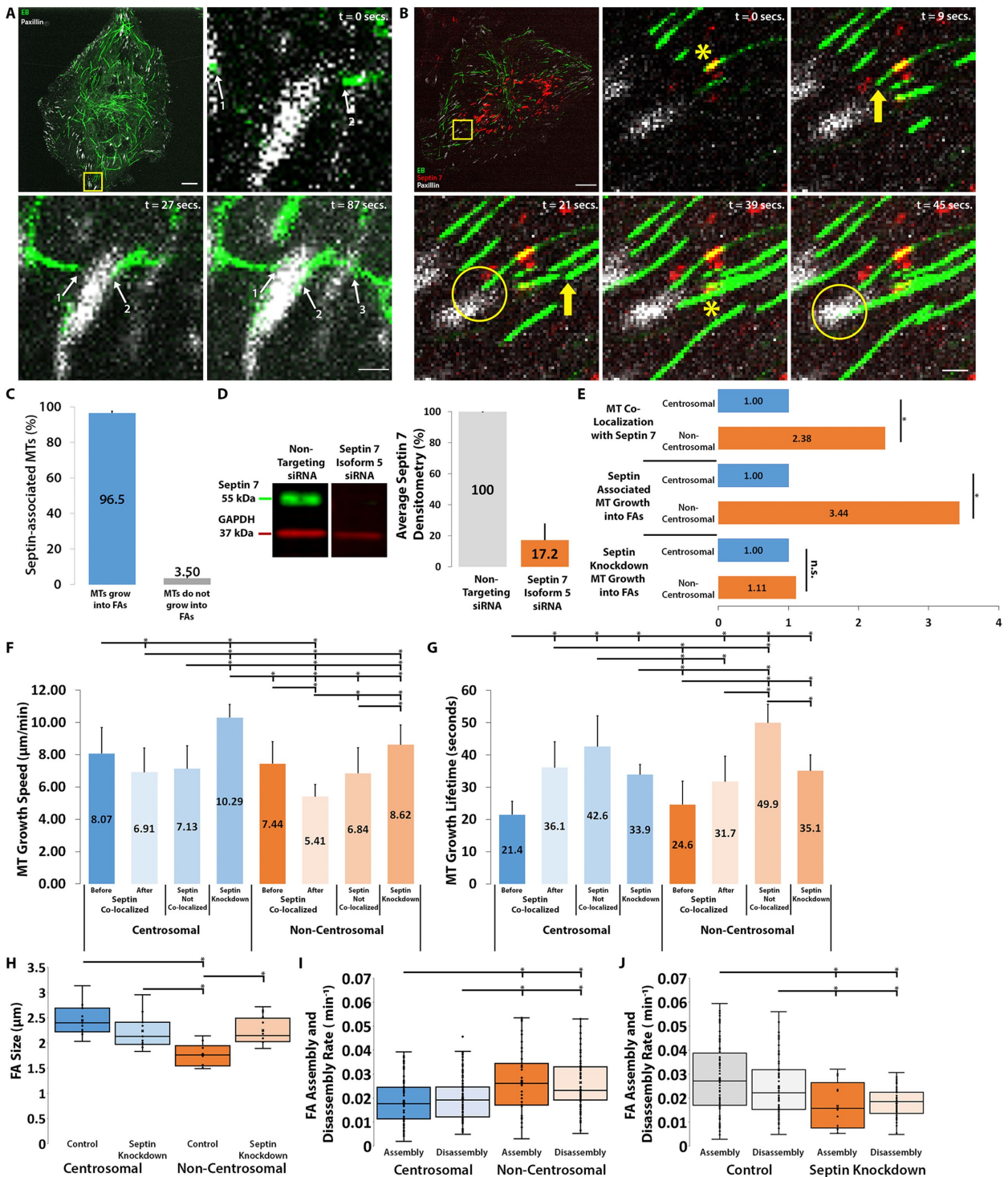
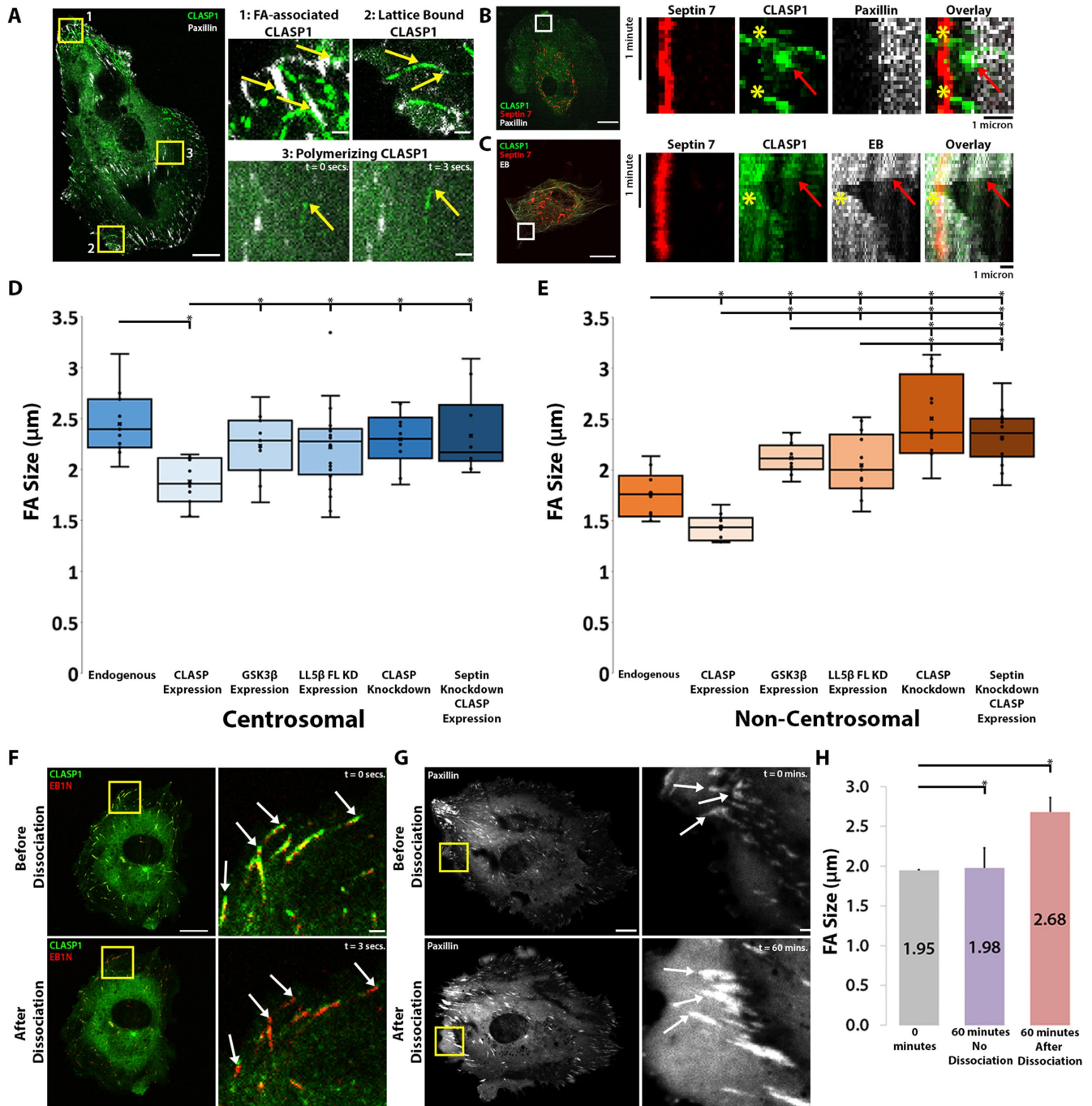


FIGURE 2: Septin directs NC MTs to FAs and regulates FA dynamics. (A) HUVEC expressing GFP-EB3 and white FAs (paxillin). Zoomed region (yellow box) showing max-intensity time-lapse images of MTs polymerizing into FAs. White arrows indicate the plus ends of different MTs that polymerize into FAs. (B) HUVEC expressing GFP-EB3 (green), mCherry-Septin 7 (red), and paxillin (white). The assembling MT (yellow arrow) grows toward Septin 7, colocalizes with Septin 7 (yellow asterisk), and changes trajectory while continuing to polymerize into a FA (yellow circle; related to Supplemental Video 3). (C) Quantification of phenomenon described in B. (D) Septin 7 KD verification of Septin 7 Isoform 5 compared with a nontargeting control. Densitometry an average of three replicates. (E) Quantification of MT colocalization with Septin 7 (top), Septin 7-associated MT growth into FAs (middle), and MT growth into FAs, comparing centrosomal and NC MTs. (F, G) Measurement of MT growth speed (F) or MT growth lifetime (G) comparing centrosomal and NC MTs that colocalized with Septin 7, those that did not colocalize with Septin 7, and MTs with septin KD. (H) Comparison of FA size between control and Septin KD conditions. (I–J) Focal adhesion analysis of assembly and disassembly between centrosomal and NC (I) and control and Septin KD cells (H). Error bars show \pm SE in C and \pm SD in D, F, and G. Scale bars = 10 μm , whole cell view; 1 μm , zoomed view. Student's *t* test; *p* (*) < 0.05.



dynamics, and was sufficient to drive FA disassembly (Stehbens *et al.*, 2014). To distinguish between the effects of FA-associated CLASP and MT-associated CLASP on FA size, we compared LL5 β FL KD (which removes FA-CLASP; Stehbens *et al.*, 2014; Lim *et al.*, 2016) to expression of GSK3 β , the kinase that inhibits MT-CLASP localization and activity (Wittmann and Waterman-Storer, 2005; Kumar *et al.*, 2009) and compared these to CLASP KD. These experiments confirmed that LL5 β FL KD resulted in increased FA size but also revealed that GSK3 β increased FA size in the NC MT group only (comparing Figure 3, D and E). CLASP KD resulted in FA sizes similar to those of endogenous controls in the centrosomal MT group (CLASP KD = 2.30 μ m; centrosomal endogenous = 2.44 μ m; Figure 3D) but resulted in a dramatic and statistically significant increase in FA size in the NC MT group (CLASP KD = 2.50 μ m; NC endogenous = 1.76 μ m; Figure 3E). In both the centrosomal MT group and the NC MT group, CLASP expression did not alter FA size in the absence of Septin 7 (septin KD CLASP expression = 2.33 μ m [centrosomal] vs. 2.32 μ m [NC]; Figure 3, D and E). To further investigate the behaviors of MT-associated CLASP, we introduced an EB1 construct (π -EB1; Van Haren *et al.*, 2018) that disrupts CLASP binding to MT plus ends upon exposure to 405 nm wavelength of light (EB1N; Figure 3F). Optogenetic dissociation of EB-bound CLASP revealed that FA size increased by 26.1% (1.98 μ m before dissociation vs. 2.68 μ m after dissociation; Figure 3, G and H). Taken together, these results indicate that CLASP localizes to Septin 7-associated MTs as they polymerize into FAs, that MT-associated CLASP promotes FA size reduction, and that CLASP-mediated control of FA size involves both FA-associated CLASP and MT-associated CLASP.

MCAK and Aurora-A control the dynamics of septin-associated MTs to regulate FA size

Our data indicated that septins may regulate NC MT growth speed to guide MT growth into FAs and that CLASP promotes septin-associated MT assembly and rescue, resulting in reduced FA size. EC polarization and directional migration is known to be controlled through localized regulation of the MT depolymerizing kinesin, MCAK, through a Rac1 and Aurora-A kinase signaling mechanism (Braun *et al.*, 2014). Additionally, septins have been shown to promote MT growth by suppressing MT catastrophe (Bowen *et al.*, 2011; Bai *et al.*, 2016; Nakos *et al.*, 2019; Spiliotis and McMurray, 2020). Thus, we posited that, in addition to regulating NC MT polymerization rates, peripheral septins may protect NC MTs from depolymerization to enhance MT growth into FAs. To test this hypothesis, we performed time-lapse imaging with the MT-depolymerizing enzyme, MCAK, Septin 7, and either EB3 to label MT plus ends or paxillin to label FAs. Live-cell imaging confirmed that MCAK labels and tracks with the plus ends of both centrosomal and NC MTs (Figure 4A; Lee *et al.*, 2008; Marvin *et al.*, 2011; Zong *et al.*, 2021). Kymograph analysis of NC MCAK-labeled MT dynamics revealed significant changes in growth dynamics before and after colocalization with peripheral septins. Septin-associated MTs were observed to undergo MCAK-associated catastrophe beginning within the FA and then terminating at the distal edge of the peripheral septin. These catastrophe events were typically followed by MT rescue and growth back into the same FA (Figure 4B). Measurements of septin-associated, MCAK-labeled MT polymerization revealed that the average time of MT polymerization from Septin 7 to FAs was 29.1 s, with an average MT dwell time of 11.8 s at the FA. MCAK-induced MT disassembly from the FA back to the peripheral septin resulted in a pause of MT dynamics that lasted, on average, 29.2 s, followed by rescue and regrowth into the FA (Figure 4C). Together, these data

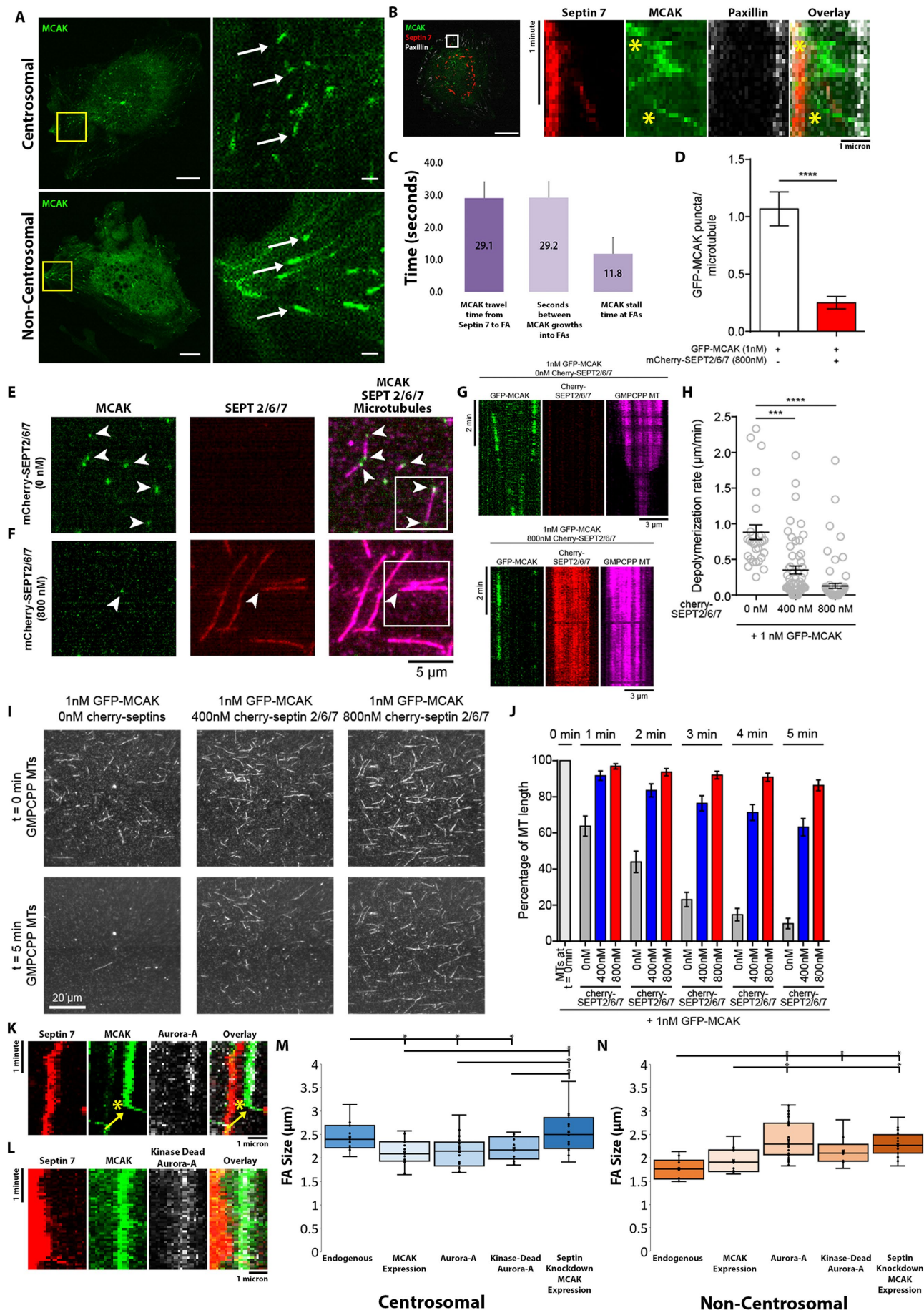
indicate that peripheral septins inhibit MCAK-mediated disassembly of NC MTs.

To determine the capacity for septin oligomers to inhibit MCAK-driven MT disassembly, we performed *in vitro* MT depolymerization assays using GMPCPP MT seeds in the presence or absence of 1 nM GFP-MCAK and either 400 or 800 nM mCherry-labeled Septin 2/6/7 complex. These experiments revealed that the presence of Septin 2/6/7 on MTs influenced the amount of MCAK that localized to the MT ends (puncta/MT; Figure 4, D–F, and Supplemental Videos 4 and 5). Kymograph analysis further revealed that in the absence of septins, MCAK completely disassembled the GMPCPP-labeled MTs at a depolymerization rate of 0.85 μ m/min, while addition of Septin 2/6/7 resulted in a potent inhibition of MT disassembly by MCAK in a concentration-dependent manner (Figure 4, G and H). *In vitro* analysis of MT length revealed that MTs were reduced by >90% after a 5-min incubation with 1 nM MCAK, while the addition of the Septin 2/6/7 complex at 400 and 800 nM concentrations rescued MT length to 65% and 85% of controls, respectively (Figure 4, I and J). These data reveal that MT-bound septin is sufficient to inhibit MCAK-mediated MT disassembly.

Coexpression of Septin 7 with MCAK and Aurora-A (a kinase that inhibits MCAK depolymerase activity; Zhang *et al.*, 2008; Xia *et al.*, 2014) revealed that Aurora-A consistently colocalized to the distal edge of peripheral Septin 7, the same site where Septin 7-associated NC MTs were observed to undergo rescue (Figure 4K), suggesting that inhibitory phosphorylation of MCAK by Aurora-A kinase may be controlling NC MT dynamic instability. Comparison of these data to a kinase-dead Aurora-A mutant expression construct revealed that both the wild-type and kinase-dead Aurora-A proteins localized to MT plus ends at the distal edge of Septin 7 (Figure 4, K and L, and Supplemental Figure S2F). However, in the absence of Aurora-A-mediated inhibition of MCAK (Aurora-A mutant), Septin 7-associated MTs underwent MCAK-driven disassembly that was stalled at the distal end of Septin 7 and did not undergo subsequent rescue as was observed in the presence of the wild-type Aurora-A construct (Figure 4, K and L). Comparison of FA sizes under these conditions revealed that in ECs with centrosomal-only MTs, FA size was mildly reduced under conditions of MCAK expression, but this effect was not altered by coexpression of either wild-type Aurora-A or mutant Aurora-A (Figure 4M). For NC MTs, MCAK expression alone did not significantly alter FA size, but expression of Aurora-A resulted in significantly increased FA size compared with endogenous control or MCAK alone (Figure 4N). These effects of MCAK inhibition on FA size were further confirmed by expressing a nonphosphorylatable MCAK mutant (active MCAK) or a phosphomimetic MCAK (inactive MCAK; see Supplemental Figure S2G). KD of Septin 7 resulted in FA sizes that were similar to those of endogenous FAs in the centrosomal-only group and that were significantly larger than endogenous in the NC MT group (Figure 4, M and N). These data indicate that Aurora-A kinase promotes rescue of MCAK-disassembled, septin-associated NC MTs to regulate FA size.

CLASP and MCAK cooperate to control septin-associated NC MT dynamics

Our data suggested that both CLASP and MCAK were contributing to the behaviors of Septin 7-associated NC MT and FA dynamics. Therefore, to visualize the localization and dynamics of Septin 7, CLASP, MCAK, and FAs, we performed kymograph analysis of septin-associated NC MT polymerization. These data revealed that rescue of MCAK-induced MT disassembly occurred at the distal end of peripheral Septin 7 and coincided in both time and space with



CLASP labeling of the MT lattice (Figure 5A). Importantly, we did observe instances where peripheral Septin 7 did not display CLASP accumulation, and in these cases as well as in conditions of CLASP KD (Supplemental Figure S2H), MCAK-disassembled MTs would stall at the distal end of the Septin 7 (similar to the Aurora-A mutant; Figure 4L), providing further support that at least one role of Septin 7 is to inhibit MCAK-mediated MT disassembly (Figure 5B). Furthermore, kymograph analysis of septin-associated NC MT assembly into FAs revealed that in the presence of both MCAK and CLASP, CLASP-labeled MTs would assemble into the FA, the CLASP would then disappear, and then the MCAK-labeled MT would disassemble back to the septin (Figure 5C, double arrow). Quantification of CLASP- and/or MCAK-labeled MTs revealed that the relative positions of FAs and FA-proximal septins ranged from 5.82 to 3.72 μm under conditions of CLASP expression or MCAK expression, respectively (Supplemental Figure S2I). Measurements of MT polymerization from septin to FAs identified that MTs containing both CLASP and MCAK were the predominant population observed to polymerize from FA proximal septins into FAs (83.7%), while MTs labeled with only CLASP polymerized from septins into FAs 16.3% of the time (Figure 5D). MTs containing only MCAK were unable to polymerize from the FA proximal septin (Figure 5D) but remained stalled at the distal end of the septin (as depicted in Figure 5B). Taken together, these data indicate that MCAK and CLASP function cooperatively with peripheral septin-associated MTs to drive the dynamic interactions between NC MTs and FAs.

To investigate the individual contributions of MCAK and CLASP to FA size, we evaluated NC MT dynamics under conditions where MT-associated CLASP or MCAK was inhibited. We had previously identified that expression of wild-type Aurora-A kinase was sufficient to inhibit MCAK depolymerase activity in ECs (Braun *et al.*, 2014). Using this approach, we performed live-cell confocal imaging and analyzed the behaviors of MTs, septin, and FAs. The combination of CLASP and wild-type Aurora-A resulted in the stabilization of septin-associated NC MTs (Figure 5E). CLASP expression with kinase-dead Aurora-A (MCAK-active condition) reduced CLASP accumulation along MTs between Septin 7 and the peripheral FA and increased CLASP localization adjacent to FAs (Figure 5F), similar to what we and others have previously classified as FA-associated CLASP (Figure 3A; Stehbins *et al.*, 2014). In another set of experiments, we combined expression of MCAK with GSK3 β expression to inhibit MT-associated CLASP. Under these conditions MCAK-

labeled MT plus ends were observed as short puncta that remained static near the peripheral Septin 7 or that were actively undergoing disassembly and unable to elongate into FAs (Figure 5G). Conversely, inhibition of FA-associated CLASP by LL5 β KD (Stehbins *et al.*, 2014) promoted increased MCAK labeling of MTs that subsequently colocalized with both Septin 7 and FAs (Figure 5H).

Quantification of FA size revealed that, for centrosomal MTs, the combination of LL5 β depletion and MCAK expression or the combination of wild-type or kinase-dead Aurora-A with CLASP expression resulted in FA sizes indistinguishable from those of endogenous controls (Figure 5I). Moreover, in cells with centrosomal-only MTs, the FA sizes were similar to measurements of FAs in cells with all MTs (Supplemental Figure S3), indicating that the effects of CLASP and MCAK on centrosomal MTs may potentially contribute to reductions in FA size through a FA CLASP-mediated MT capture mechanism (Stehbins *et al.*, 2014). For NC MTs, MCAK expression under conditions of LL5 β depletion increased FA size consistent with LL5 β KD alone (2.04 μm in both cases; see also Figure 3E). MCAK expression under conditions of MT-associated CLASP inhibition (GSK3 β) resulted in the largest FA sizes (2.50 \pm 0.11 μm). Coexpression of CLASP and active Aurora-A (to inhibit MT-associated MCAK activity) resulted in FA sizes indistinguishable from MCAK expression alone, while coexpression of CLASP with kinase-dead Aurora-A resulted in FA sizes similar to MCAK inhibition alone (2.29 μm ; Figure 5J vs. 2.38 μm ; Figure 4N). These data indicate that the activity of both CLASP and MCAK on NC MTs is essential to promoting reduced FA size. In CLASP-inhibited cells, MCAK-mediated MT disassembly is enhanced and septin-associated MT rescue is limited, while, in MCAK-inhibited cells, CLASP-mediated MT assembly is enhanced and FA-associated MT disassembly is reduced, with both conditions promoting increased FA size.

Rac1 promotes septin filament assembly proximal to peripheral FAs

Integrin engagement of the ECM induces the formation of nascent FAs and locally activates the small GTPase, Rac1 (Gardel *et al.*, 2010; Parsons *et al.*, 2010). Rac1 activity is known to trigger localized actin and MT assembly, resulting in cell protrusion that defines the leading edge and drives polarization and motility (Van Aelst and D'Souza-Schorey, 1997; Nobes and Hall, 1999; Waterman-Storer and Salmon, 1999; Waterman-Storer *et al.*, 1999; Grabham, 2003; Wittmann *et al.*, 2003; Wittmann and Waterman-Storer, 2005).

FIGURE 4: MCAK and Aurora-A control the dynamics of septin-associated MTs to drive FA disassembly. (A) HUVEC expressing GFP-MCAK in conditions of centrosomal (top row) or NC (bottom row) MTs. (B) Whole-cell view with white box indicating region of kymograph. Representative kymograph of GFP-MCAK, mCherry-Septin 7, and paxillin (white) showing MT dynamics between Septin 7 and a FA. Growth events labeled with yellow asterisk. (C) Analysis of MCAK-labeled NC MT average time of growth from Septin 7 to FAs, time between growth excursions into FAs, and time spent at FAs. (D) Measurement of average GFP-MCAK puncta per MT in the presence or absence of mCherry-Septin 2/6/7 in vitro. (E, F) Still images of in vitro HiLyte-647-GMPCPP-stabilized MTs with purified GFP-MCAK in the absence (E) or presence (F) of mCherry-Septin 2/6/7 complex. White boxes represent the MTs used in G; related to Supplemental Videos 4 and 5). (G) Representative kymographs showing in vitro depolymerization assays with HiLyte-647-GMPCPP-stabilized MTs with purified GFP-MCAK without (top) and with (bottom) mCherry-SEPT2/6/7 complex. (H) Quantification of MCAK-mediated depolymerization rates for conditions described in E–G. (I) Time-lapse images showing in vitro depolymerization assays with HiLyte-647-GMPCPP-stabilized MTs with purified GFP-MCAK and increasing concentrations of mCherry-SEPT2/6/7. (J) Analysis of MT length measurements from experiments in I. (K, L) Representative kymographs of either wild-type Aurora-A kinase (white; K) or a kinase-dead Aurora-A mutant (white; L) with mCherry-Septin 7 and GFP-MCAK showing that the wild-type Aurora-A kinase accumulates and drives rescue of MCAK-labeled MTs at the distal edge of peripheral Septin 7 (yellow asterisk and yellow arrow; K). (M, N) Comparison of FA size between endogenous control cells and cells expressing either MCAK, Aurora-A kinase, the kinase-dead Aurora-A mutant with centrosomal (M) or NC (N) MTs. Error bars show \pm SE in C, F, G, and I. Scale bars = 10 μm , whole-cell view; 1 μm , zoomed view. Student's *t* test; *p* (*) < 0.05; *p* (***) < 0.001, *p* (****) < 0.0001.

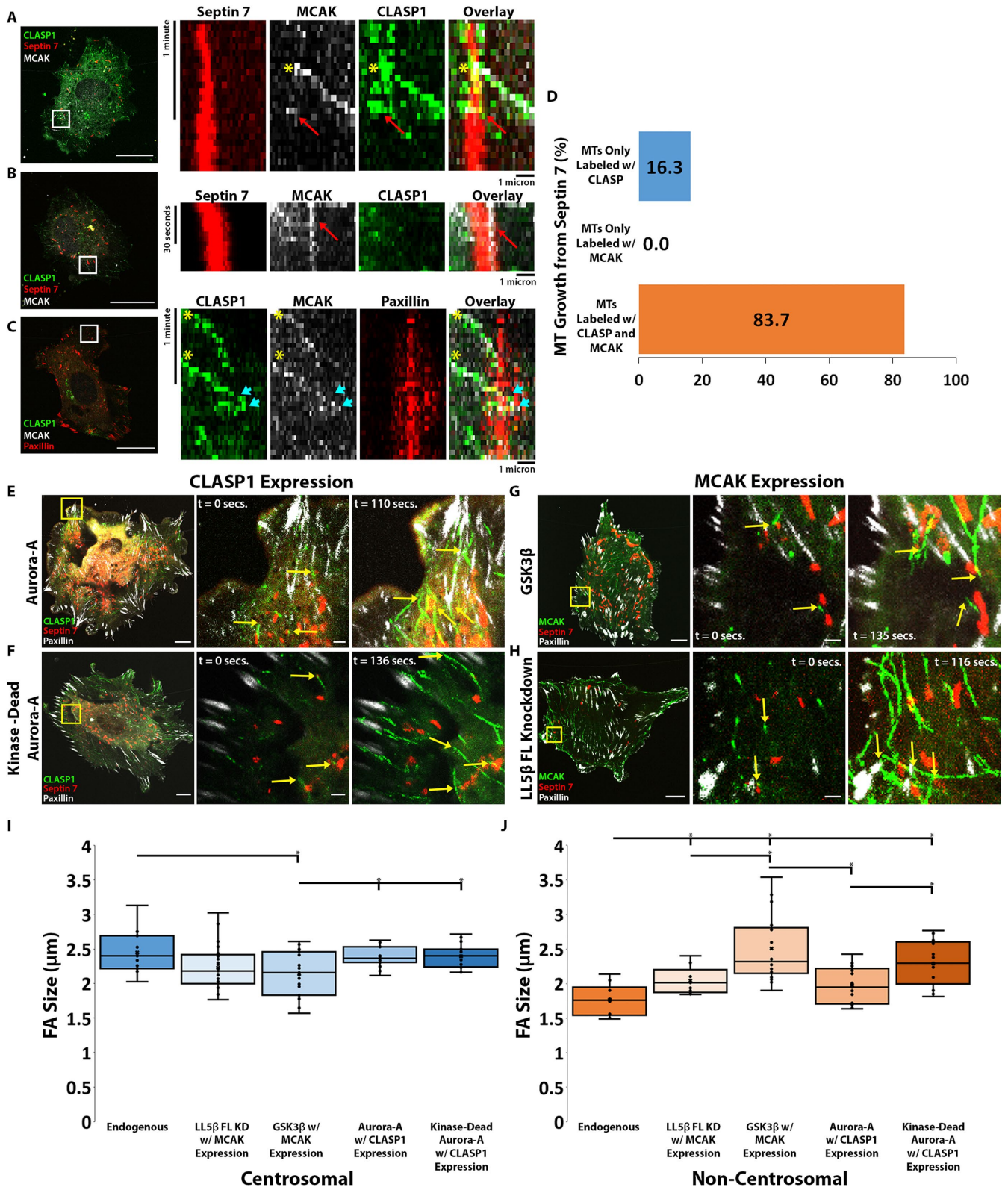


FIGURE 5: CLASP and MCAK cooperate to control septin-associated NC MT dynamics to regulate FA size. (A, B) Representative kymographs showing behaviors of MCAK and CLASP dynamics relative to peripheral mCherry-Septin 7 with CLASP accumulation (A) or in the absence of CLASP accumulation (B). Whole-cell images to the left show the region of the kymograph (white box). Yellow asterisks indicate copolymerization of MCAK and CLASP adjacent to septin, and red arrows indicate MCAK disassembly back to Septin 7. (C) Representative kymograph showing behaviors of MCAK and CLASP dynamics relative to FAs (mApple-paxillin). Yellow asterisks indicate copolymerization of MCAK and CLASP that terminates within the FA (blue arrows). Whole-cell image to the left shows the region of the kymograph (white box). (D) Comparison of MT growth from Septin 7 between MTs that have CLASP only, MCAK only, or CLASP and

Additionally, Rac1 is known to control the function of CLASP and MCAK activity indirectly by activating their regulatory kinases, GSK3 β and Aurora-A, respectively (Wittmann and Waterman-Storer, 2005; Rannou *et al.*, 2008; Lorenzo *et al.*, 2009).

To determine the effects of Rac1 activity on Septin 7 organization and consequences for centrosomal versus NC MTs and FA size, we used a dominant-negative Rac1 (DN-Rac1) and a constitutively active Rac1 (CA-Rac1; Schnelzer *et al.*, 2000; Aoki *et al.*, 2004), which function globally within the cell, as well as a photoactivatable Rac1 (PA-Rac1; Wu *et al.*, 2009) that can be locally activated in distinct subcellular regions. Measurements of Septin 7 localization revealed that the peripheral Septin 7 was significantly increased in the CA-Rac1 condition compared with both endogenous Rac1 and the DN-Rac1 conditions (Figure 6, A and B). Localized photoactivation of Rac1 was sufficient to drive the reorganization of Septin 7 filaments to the region of the cell where Rac1 was activated (Supplemental Video 6). Moreover, optogenetic activation of Rac1 induced the assembly of FA-proximal septin filaments that could be relocated by activating Rac1 in a different subcellular region (Figure 6C). Comparison of FA size within the region of Rac1 photoactivation (Figure 6D) to adjacent regions where Rac1 was not photoactivated revealed a persistent, four-fold reduction in FA size within the PA-Rac1 region, while in adjacent regions, FA size remained essentially unchanged (Figure 6E). These results indicate that Rac1 activity promotes the accumulation of peripheral Septin 7 proximal to FAs and contributes to reductions in FA size.

Septin effects on NC MT growth into FAs are dependent on acto-myosin contractility

Septins are well understood to bind to both MTs and actin filaments. Peripheral septins localize adjacent to FAs and contribute to the stabilization of nascent FAs (Dolat *et al.*, 2014), and evidence supports a role for septins impacting the activity of the myosin-II motor protein via binding of actin stress fibers (Smith *et al.*, 2015). Additionally, FA-associated actin stress fibers are known to be necessary for MT growth into FAs and myosin-II contractility is required for force-driven FA turnover in other cell types (Vicente-Manzanares *et al.*, 2009; Rafiq *et al.*, 2019).

We first investigated the effects of pharmacologic disassembly of actin filaments following treatment with latrunculin on Septin 7 organization. These experiments revealed that most of Septin 7 withdrew from the cell periphery as actin filaments disassembled, except in cases where septins were colocalized with MTs before the addition of latrunculin (Figure 7A). Pharmacologic disassembly of MTs via treatment with nocodazole was associated with hypercontractility of actin fibers (as previously reported; Liu *et al.*, 1998) and resulted in increased lateral movement of the septin but generally did not cause the septin to leave the cell periphery (Figure 7B). To determine the contribution of myosin-II contractility to peripheral septin localization, cells were treated with blebbistatin and Septin 7 localization was again analyzed. Similar to the latrunculin experiment, myosin-II inhibition resulted in the withdrawal of peripheral

septins except for those that were colocalized with MTs before the addition of blebbistatin (Figure 7C). Evaluation of MTs and FAs revealed that septin-colocalized MTs consistently assembled beyond nearby FAs following myosin-II inhibition (Figure 7D). Together, these data indicate that the peripheral localization of Septin 7 depends primarily on the structural integrity of actin filaments, and secondarily upon colocalization with MTs.

To determine the effects of acto-myosin contractility on MT-FA behavior, we measured peripheral Septin 7 (Figure 7E), MT growth into FAs (Figure 7F), and effects on FA size (Figure 7G), comparing before and after myosin-II inhibition. Because prolonged (30–60 min) blebbistatin-induced myosin-II inhibition results in near complete FA disassembly independent of MTs (Wolfenson *et al.*, 2011), we used a 15 min treatment with 20 μ M blebbistatin that is sufficient to inhibit myosin-II contractility (IC50 ~5.1 μ M; Limouze *et al.*, 2004) but without driving the removal of the FA marker paxillin from FAs (Wolfenson *et al.*, 2011). Measurements revealed that myosin-II inhibition resulted in a loss of 45.1% of peripheral Septin 7 in the NC MT group, resulting in a myosin-II-inhibited peripheral Septin 7 count for both centrosomal and NC MTs similar to that of centrosomal MTs before blebbistatin treatment (Figure 7E). Measurements of MT growth into FAs revealed that myosin-II inhibition significantly reduced septin-associated assembly of NC MTs into FAs (58% reduction), while centrosomal MT growth into FAs was reduced but not significantly altered (10% reduction; Figure 7F). Analysis of FA size before and after inhibition of myosin-II contractility revealed that FA size was increased by 22% in cells with NC-only MTs, while in cells with centrosomal-only MTs, FA sizes were unaffected by myosin-II contractility (Figure 7G). These data indicate that myosin-II contractility may work in concert with septin-associated NC MTs to control FA dynamics.

To determine the combined effects of Rac1 activation and myosin-II contractility, we photoactivated Rac1 within peripheral regions of the cell and performed temporal measurements of FA size and peripheral Septin 7 count within the PA-Rac1 regions (Figure 7H). These data revealed that the effects of Rac1 activation on peripheral Septin 7 accumulation and on FA size in blebbistatin conditions were dramatically reversed when compared with Rac1 activation in the presence of myosin-II contractility (comparing Figures 6E and 7H). In the absence of myosin-II contractility, Rac1 activation was insufficient to retain peripheral Septin 7, resulting in the withdrawal of approximately two-thirds of the peripheral Septin 7 within 1 h of blebbistatin treatment and that FA sizes were statistically similar both within and outside the region of Rac1 activation (Figure 7H). Together, these data point to acto-myosin contractility as a prerequisite for NC MT interactions with peripheral septins, for growth into FAs, and for the maintenance of FA size.

Septin-mediated guidance of NC MTs promotes polarized EC migration

In a final set of experiments, we set out to determine the consequences of septin and NC MT growth into FAs on EC migration

MCAK labeling coming from Septin 7 (percent). (E, F) Still images from a time-lapse experiment showing HUVECs expressing GFP-CLASP1, mCherry-Septin 7, and paxillin (white) with Aurora-A kinase (E) or kinase-dead Aurora-A mutant (F) showing CLASP localization (yellow arrows) relative to Septin 7 (red). (G) HUVECs expressing GFP-MCAK, mCherry-Septin 7, and paxillin (white) with GSK3 β or (H) LL5 β KD showing MCAK localization (yellow arrows) relative to Septin 7 (red). (I, J) Comparison of FA size between endogenous control cells and cells expressing either LL5 β KD with MCAK, GSK3 β with MCAK, Aurora-A kinase with CLASP, or the kinase-dead Aurora-A mutant with CLASP expression in cells with centrosomal (I) or NC (J) MTs. Scale bars = 20 μ m, whole-cell view for kymographs; 10 μ m, whole-cell view; 1 μ m, zoomed view. Student's *t* test; *p* (*) < 0.05.

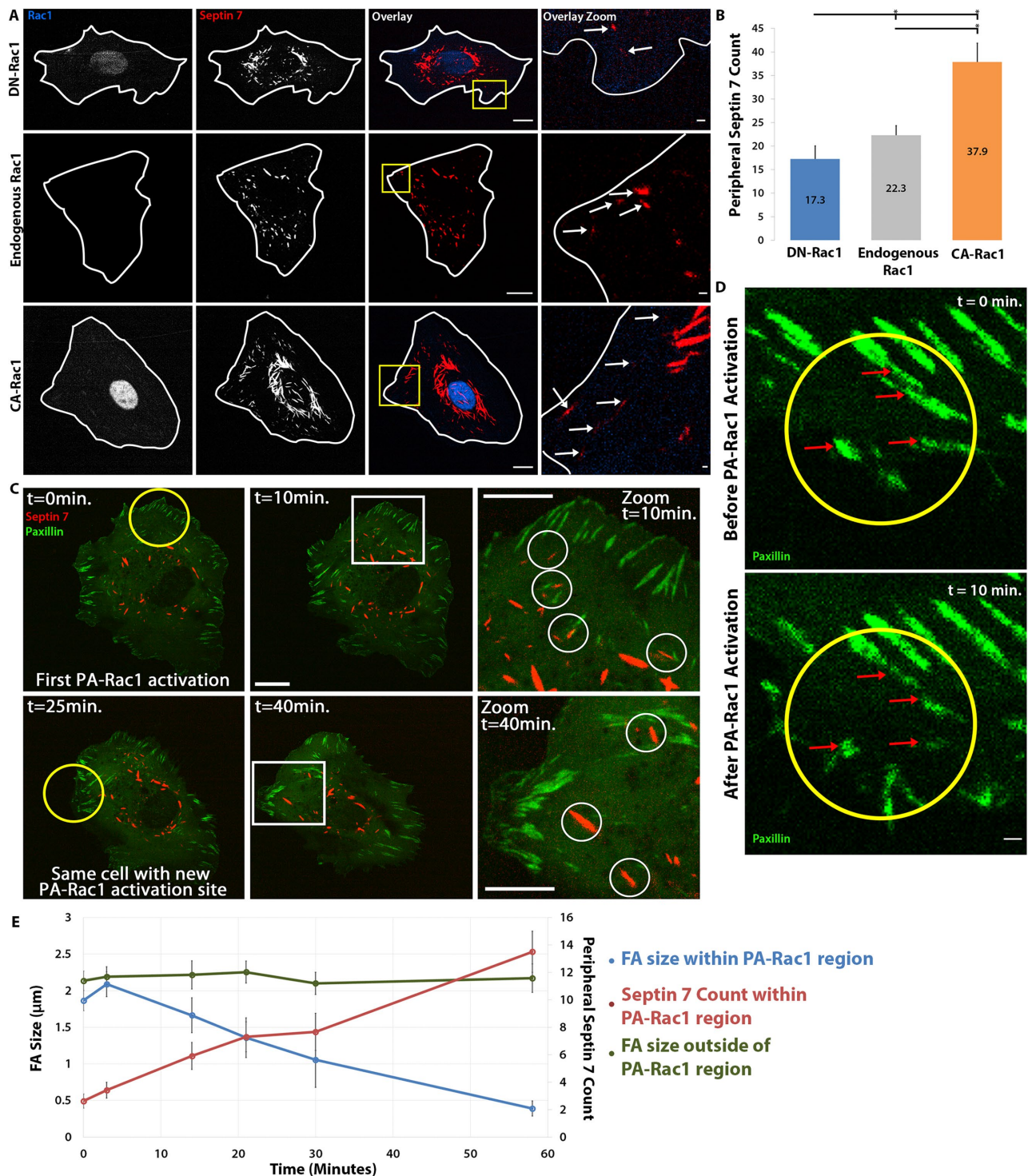


FIGURE 6: Rac1 promotes septin filament assembly proximal to peripheral FAs. (A) HUVECs expressing mCherry-Septin 7 and dominant negative Rac1 (DN-Rac1; top row), endogenous Rac1 (middle row), or constitutively active Rac1 (CA-Rac1; bottom row). Zoom regions (yellow boxes) show peripheral Septin 7 localization (white arrows in overlay zoom). (B) Quantification of peripheral Septin 7 in conditions shown in A. (C) HUVEC expressing GFP-paxillin and mCherry-Septin 7 with unlabeled-PA (photoactivatable) Rac1. (Top row) Time-lapse images showing a region of Rac1 photoactivation (yellow circle) at $t = 0$ min. Zoom region (white box) showing the assembly of mCherry-Septin 7 filaments proximal to peripheral FAs at $t = 10$ min (white circles). (Bottom row) Time-lapse images showing a region of Rac1 photoactivation (yellow circle) at $t = 25$ min. Zoom region (white boxes) showing assembly of Septin-7 filaments proximal to peripheral FAs at $t = 40$ min (white circles) within a second localized region of the same cell (related to Supplemental Video 6). (D) Time-lapse images showing FA disassembly following Rac1 photoactivation (yellow circles). Red arrows indicate the same FAs before and after Rac1 photoactivation. (E) Quantification of peripheral Septin 7 (red) and FA size (blue) within regions of Rac1 photoactivation and compared with FA size outside of regions of Rac1 photoactivation (green). Error bars show \pm SD. Scale bars = 10 μ m, whole-cell view; 1 μ m, zoomed view. Student's t test; p (*) < 0.05.

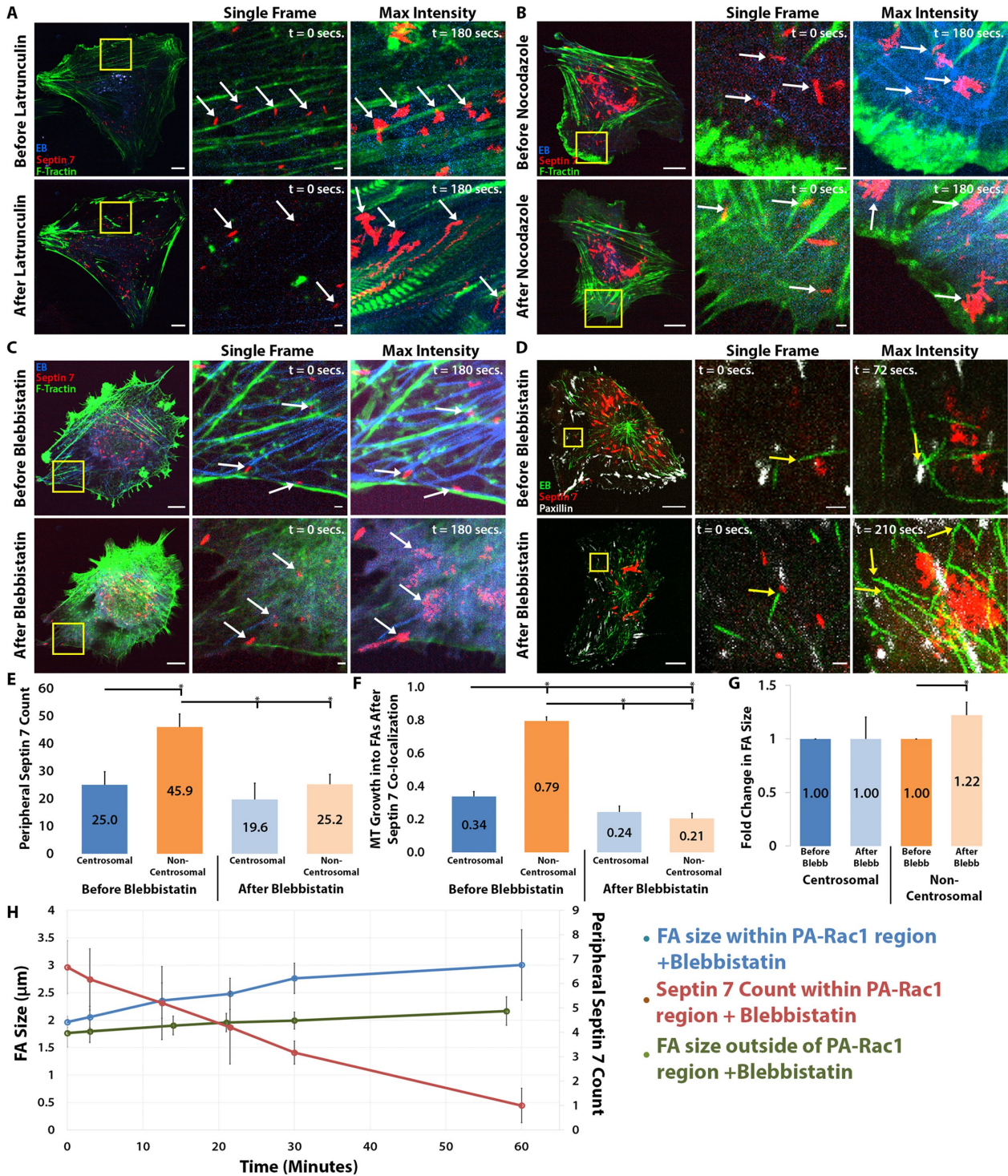


FIGURE 7: Septin effects on NC MT growth into FAs are dependent upon acto-myosin contractility. (A) HUVEC expressing GFP-F-Tractin, mCherry-Septin 7, and BFP-EB3 showing the effects on Septin 7 localization following the addition of (A) latrunculin (to disassemble actin filaments); (B) nocodazole to disassemble MTs; (C, D) blebbistatin to inhibit myosin-II contractility and actin organization (C) or FA organization (D) EB (green), Septin 7 (red), and FAs (paxillin; white). Yellow box indicates zoomed region. White arrows in A, B, and C track peripheral Septin 7 before and after treatment. Yellow arrows in D show growth of Septin 7 colocalized MTs into a FA before treatment and loss of growth into FAs after treatment. (E) Peripheral Septin 7 count before and after myosin-II inhibition in cells under conditions of centrosomal or NC MTs. (F) Analysis of MT growth into FAs after Septin 7 colocalization before and after myosin-II inhibition between centrosomal and NC MTs. (G) Quantification of FA size after myosin-II inhibition in cells under conditions of centrosomal (left) or NC (right) MTs. (H) Quantification of peripheral Septin 7 count (red) and FA size (blue) within the region of Rac1 photoactivation and compared with FA size outside of regions of Rac1 photoactivation (green) following myosin-II inhibition with blebbistatin. Error bars show \pm SD. Scale bars = 10 μ m, whole-cell view; 1 μ m, zoomed view. Student's *t* test; *p* (*) < 0.05.

using a wound-healing migration assay. NC cells showed a relatively uniform and polarized wound edge and consistently migrated into and across the wound, while centrosomal cells displayed disorganized polarity and were observed to migrate with reduced directional persistence (Figure 8A). Consistent with previous findings (Martin *et al.*, 2018), our measurements of wound closure speed revealed that NC cells migrated faster and with greater persistence than centrosomal ECs (NC = 44.5 $\mu\text{m}/\text{h}$, centrosomal = 16.5 $\mu\text{m}/\text{h}$; Figure 8B).

To assay the effects of CLASP and MCAK on NC MT cell migration, we again performed the wound-healing assay under conditions of CLASP inhibition by GSK3 β , MCAK inhibition by wild-type Aurora-A kinase, or conditions of CLASP or Septin 7 KD. In each condition for NC MTs, wound closure speed decreased compared with control, with the Septin-7 KD condition displaying the slowest migration rate (Control = 44.5 $\mu\text{m}/\text{h}$; Aurora-A = 16.0 $\mu\text{m}/\text{h}$; GSK3 β = 19.6 $\mu\text{m}/\text{h}$; CLASP KD = 26.3 $\mu\text{m}/\text{h}$; Septin 7 KD = 10.5 $\mu\text{m}/\text{h}$; Figure 8, A and B). Comparing these same experimental groups in ECs with centrosomal-only MTs, no significant differences were measured (Control = 16.5 $\mu\text{m}/\text{h}$; Aurora-A = 19.1 $\mu\text{m}/\text{h}$; GSK3 β = 23.5 $\mu\text{m}/\text{h}$; CLASP KD = 11.5 $\mu\text{m}/\text{h}$; Septin 7 KD = 17.5 $\mu\text{m}/\text{h}$; Figure 8B). These data indicate that NC MTs drive EC polarity and persistent, directional wound-edge migration via a septin-CLASP- and MCAK-mediated mechanism.

To evaluate the dynamics of septins and FAs, we performed time-lapse imaging of wound-edge ECs expressing mCherry-Septin 7 and GFP-paxillin. This experiment revealed that during polarized EC migration, there is a persistent cycle of FA formation and maturation near the cell front that is followed by the appearance of Septin 7 directly proximal to mature adhesions and subsequent disassembly of the adhesion that is coupled with cell advance in the direction of the wound (Figure 8C and Supplemental Video 7).

Taken together, our data support a model for septin-mediated guidance of NC MT polymerization into FAs (Figure 8, D and E). In this model, CAMSAP stabilized NC MTs elongate toward the cell periphery. Rac1 activation near the plasma membrane promotes lamellipodial extension, FA assembly, MT polymerization, and peripheral septin localization proximal to FAs. Septin stability and maintenance within the cell periphery is controlled through the combined efforts of myosin-II contractility and FA-associated actin filaments, as well as through colocalization with NC MTs (Figure 8D). Septin-associated NC MTs assemble into adjacent FAs and undergo disassembly that is primarily driven by MCAK depolymerase activity on NC MT plus ends. One function of peripheral septin is as a physical restraint to MCAK-induced MT disassembly, thereby maintaining MT plus ends in close proximity to FAs. Septin-mediated inhibition of MT disassembly is associated with accumulation of Aurora-A kinase, which is necessary to inhibit MCAK activity and promote MT rescue. At the same time, MT-associated CLASP accumulates on septin-associated MTs to facilitate MT regrowth into the FA. Coincident loss of MT-associated CLASP and renewed MCAK activity then drive MT disassembly back to the septin once again. In this way, the positioning and function of septin enable NC MTs to undergo iterative bouts of growth and disassembly in close proximity to FAs and thereby drive FA disassembly (Figure 8E).

DISCUSSION

Spatial regulation of cytoskeletal dynamics is increasingly identified as critical to defining cell polarity and the consequences for directional cell motility. Studies in numerous different cell types now highlight that localized control of MT plus end dynamics is as essential to

the control of cell morphology during interphase as it is in regulating MT dynamics within the mitotic spindle, with many of the same regulatory proteins at work (Akhmanova and Steinmetz, 2010; Wojnacki *et al.*, 2014; Van De Willige *et al.*, 2016). A key finding was the recent discovery that the MT cytoskeleton of cells can be subdivided into centrosomal and NC groups that perform distinct functional roles. This understanding has laid the groundwork for identifying the cellular tasks accomplished by centrosomal versus NC MTs. Our findings support earlier studies (Martin *et al.*, 2018) suggesting that NC MTs are essential for driving EC front-back polarity and for polarized motility. We have identified that NC MTs accomplish this task by undergoing iterative bouts of growth and disassembly at positions directly adjacent/proximal to FAs, thereby inducing localized FA disassembly. Critical to this discovery was the finding that NC MTs preferentially colocalize with peripheral septins, which we have identified serve as a stall point for MT disassembly, thereby preventing prolonged MT shortening events and promoting MT rescue. Moreover, at the distal edge of peripheral septins we have identified a molecular skirmish whereby the iterative bouts of dynamic instability necessary to promote FA turnover are determined by the localized activity of MCAK and CLASP, as well as their regulatory kinases and the activation state of the small GTPase, Rac1.

These findings suggest mechanistic insight into decades-old experimental evidence showing that MT dynamics and growth into FAs are required for FA disassembly (Kaverina *et al.*, 1998; Ezratty *et al.*, 2005; Seetharaman and Etienne-Manneville, 2019) and more recent evidence that NC MTs carry out this function (Martin *et al.*, 2018; Rong *et al.*, 2021). Our data identify that in ECs, NC MTs preferentially polymerize into FAs followed by disassembly, while centrosomal MTs display continued assembly beyond FAs, typically terminating at the cell edge. Importantly, these data also show that greater than 95% of MTs that assembled into FAs first colocalized with peripheral septins and that MT growth trajectories were frequently altered at the site of septin-MT colocalization. These findings support previously described roles for septin-mediated MT reorganization and demonstrate for the first time that MT-induced FA disassembly is driven via septin-dependent guidance of NC MTs into FAs.

The finding that septins promote NC MT growth into FAs raises questions as to how this is accomplished. Recent studies have identified that low-concentration septin oligomers promote persistent MT growth (Nakos *et al.*, 2019), which matches what we observed for FA-proximal, septin-associated NC MTs. Previous investigations have identified that septins promote actin stress-fiber-mediated maturation of nascent focal adhesions (<1 μm), although this study did not investigate the contribution of MTs to nascent adhesion maturation (Dolat *et al.*, 2014). Our analysis of mature FA (>1 μm) kinetics suggests that the presence of FA-proximal septins serves to increase both the assembly and disassembly rates of mature adhesions (Figure 2, I and J) and further identify actin-myosin contractility as a prerequisite for NC MT effects on mature FA disassembly (Figure 7, F and G). Our studies also point to septin functioning as a restraint to NC MT disassembly and as a recruiting location for MAPs that regulate MT dynamic instability. We have previously reported on a Rac1-Aurora-A-MCAK signaling cascade as a key regulator of EC polarization and migration (Braun *et al.*, 2014). Indeed, recent investigations support the critical role of MCAK in modulating FA dynamics and cell migration, although the mechanism(s) by which MCAK functions to regulate FA dynamics was not determined (Moon *et al.*, 2021; Zong *et al.*, 2021). In this study, we have identified that MCAK-labeled NC MTs grow into FAs and then disassemble and that MCAK-mediated disassembly of septin-associated NC MTs is halted at the distal edge of peripheral septins. At the same

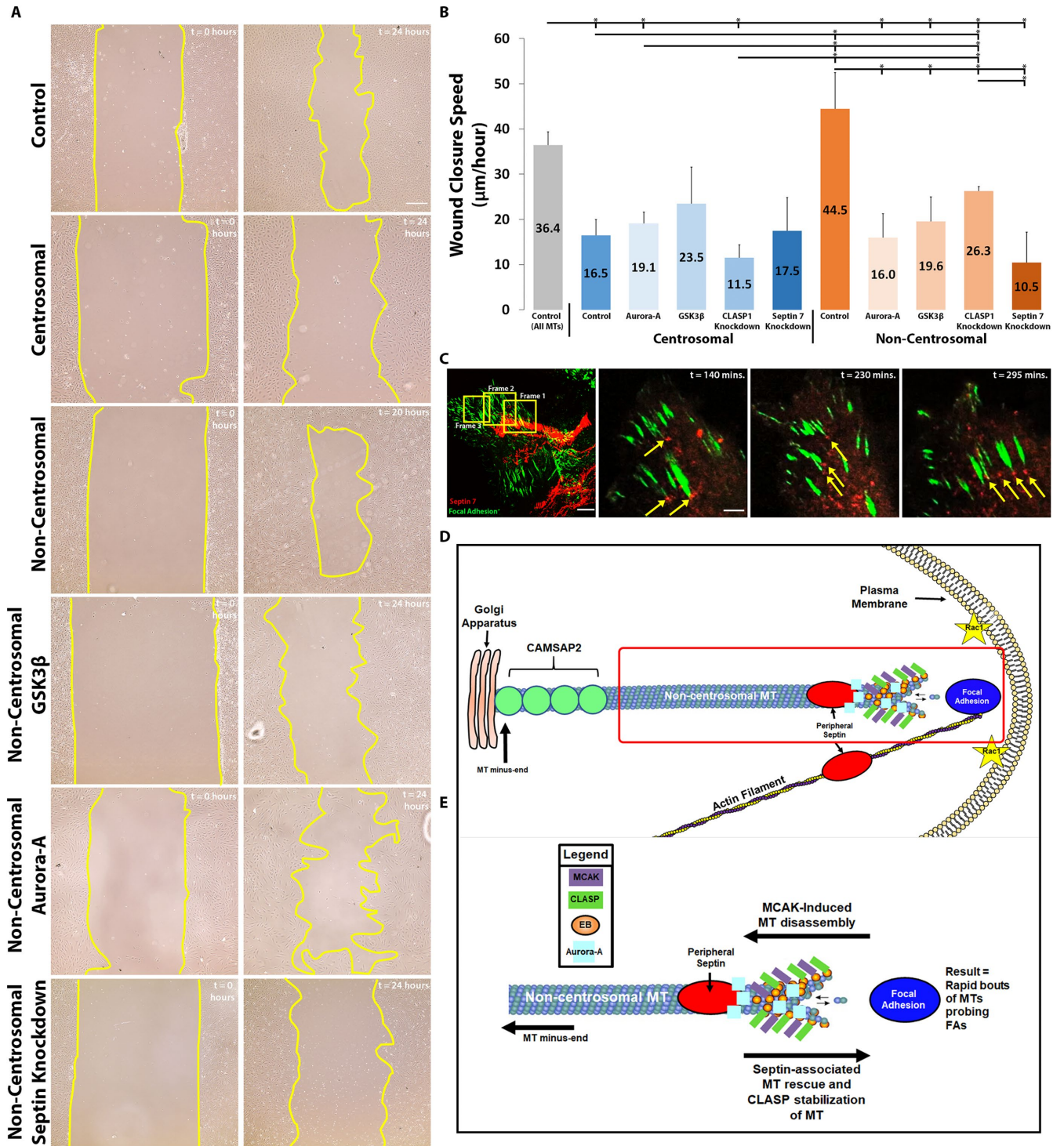


FIGURE 8: Septin-mediated guidance of NC MTs promotes polarized EC migration. (A) Time-lapse images of HUVEC wound edge migration of control (all MTs: top row), centrosomal MTs (second row), NC MTs (third row), NC MTs with GSK3 β (fourth row), NC MTs with Aurora-A kinase (fifth row), and NC MTs with Septin KD (bottom row). (B) Quantification of wound closure speed for the conditions shown in A with CLASP KD. (C) Still-frame images from a time-lapse wound edge migration experiment showing a HUVEC expressing GFP-paxillin (FAs) and mCherry Septin 7. Yellow boxes in left panel correspond to zoomed still-frame time-lapse images to the right. Yellow arrows highlight Septin 7 assembly proximal to FAs during cell migration (related to Supplemental Video 7). (D, E) Schematic diagram showing a proposed mechanism by which peripheral septins guide NC MT polymerization into FAs to promote FA disassembly and zoom (D; red box in C) of dynamic interplay between MCAK and CLASP on the MT plus tip proposed to drive FA turnover. Error bars show \pm SE. Scale bars = 500 μ m for wound edge; 10 μ m for whole-cell max intensity; 1 μ m for zoomed-in view. Student's *t* test; *p* (*) < 0.05.

location there is an accumulation of Aurora-A kinase on the MT plus end, followed by rescue of MT growth toward the FA, and the process repeats. This arrangement facilitates rapid bouts of MT assembly and disassembly directly proximal to FAs and thereby promotes FA disassembly.

The MT-associated protein CLASP has been shown to play a critical role in controlling FA capture of MTs and the subsequent delivery of matrix metalloproteases (MMPs) to facilitate FA disassembly (Stehbens *et al.*, 2014). The authors identified that FA-associated CLASP was required for MT capture but that MT dynamics were not required for CLASP-associated disassembly of FAs. It should be noted that this study did not distinguish between the NC or centrosomal origin of MTs, and so it is unclear whether one or both groups of MTs are captured by FAs. Expression of CLASP in our hands revealed localization patterns similar to those previously reported (Mimori-Kiyosue *et al.*, 2005; Miller *et al.*, 2009; Ashley *et al.*, 2014; Stehbens *et al.*, 2014; Lim *et al.*, 2016; Sanders *et al.*, 2017). However, evaluation of CLASP behavior on septin-associated NC MTs revealed that, following MCAK disassembly, rescue of MT assembly was concurrent with CLASP labeling specifically at the plus tip and along the lattice of the MT between the septin and the FA. Subsequent polymerization of the MT into the FA resulted in CLASP displacement and MCAK-associated MT disassembly that then was terminated at the septin in iterative bouts. These data support a model in which the activity states of MCAK and CLASP function like switches that turn on MT disassembly or promote stable growth, with septins spatially demarcating the switch between MCAK-driven depolymerization and CLASP-induced polymerization (Figure 8, D and E).

Rather than the prolonged capture (~18 min) of MTs at FAs identified to facilitate MMP delivery and CLASP-mediated FA disassembly (Stehbens *et al.*, 2014), our data are consistent with evidence supporting the contribution of more-dynamic MT assembly and disassembly events that result in reduced FA size (Efimov *et al.*, 2008; Efimov and Kaverina, 2009). This model fits with published work showing that MT assembly into FAs results in a sevenfold increase in the likelihood of MT disassembly (Efimov *et al.*, 2008) and with data showing that FA-associated MT disassembly drives the release of the Rho GEF-H1 from the FA milieu, thereby activating RhoA and myosin-II contractility and promoting FA turnover (Rafiq *et al.*, 2019). Yet another possible mechanism for transient MT-induced FA disassembly involves the delivery of MT end binding (EB)-associated proteins that function to promote FA turnover, such as was shown for the calcium-dependent cationic channel transient receptor potential melastatin 4 (TRPM4) protein (Blanco *et al.*, 2019). Importantly, the mechanism of septin-associated MT-driven FA turnover is not mutually exclusive from the contributions of MT capture and cargo-mediated or clathrin-mediated FA disassembly. More likely, it is the combination of these processes that enhances productive FA dynamics in order to facilitate localized ECM remodeling, acto-myosin contractility, and rapid FA disassembly as needed to promote directional cell motility.

Rac1 is a master cytoskeletal regulator that functions to drive nascent FA assembly, to promote leading edge MT growth, to target the Aurora kinases and GSK3 β , and through these various signaling cascades to be essential for cell polarity and migration (Mimori-Kiyosue *et al.*, 2005; Miller *et al.*, 2009; Stehbens *et al.*, 2014; Sanders *et al.*, 2017). In our investigation we discovered that a primary role for Rac1 is the recruitment of septin to the cell periphery, which can be driven by localized photoactivation of Rac1. While we were able to determine that the Aurora-A kinase-mediated inhibition of MCAK was important for MT rescue at the distal edge of

septins, we were not able to determine whether this was a Rac1-dependent phenomenon. Recent work looking at this signaling pathway proposed that the effects of Rac1 on MCAK-mediated MT disassembly may be independent of Aurora-A kinase, possibly working through a parallel pathway (Zong *et al.*, 2021). Our data establish one such parallel pathway in which Rac1-driven localization of peripheral septin dictates the position at which septin-associated MT dynamics are controlled to drive FA disassembly. This notion is further supported by latrunculin and blebbistatin experiments, which revealed that peripheral septin localization was reduced in the absence of actin filaments and that MT growth into FAs was reduced in the absence of myosin-II contractility. These data point to a critical role for actomyosin tensegrity and FA-coupled actin fibers in promoting septin localization near FAs, which aligns with previous studies showing that septins work to cross-link actin stress fibers and promote maturation of nascent FAs (Dolat *et al.*, 2014; Smith *et al.*, 2015).

The mechanism by which localized activation of Rac1 drives peripheral septin localization remains a mystery. However, it is possible that FA-associated alterations in membrane curvature could explain the Rac1-septin phenomenon. It is well established that septins are capable of sensing local variations in cell membrane curvature both *in vitro* (Bridges *et al.*, 2016; Beber *et al.*, 2019; Weems *et al.*, 2021; Woods and Gladfelter, 2021) and *in vivo* (Cannon *et al.*, 2019). FAs have been shown to promote high membrane curvature in an actin and myosin stress fiber-dependent manner (Novak *et al.*, 2004), which may explain the loss of peripheral septins that we observed when actin or myosin are inhibited. In fibroblasts, Rac1 has also been shown to display sensitivity to localized membrane curvature via signaling from the F-BAR-binding protein srGAP2, which resulted in Rac1 activation within a membrane band focused at the tip of contact protrusions (Rafael *et al.*, 2015). MT plus ends are known to dive down toward the dorsal membrane surface before assembling into peripheral adhesions (Krylyshkina *et al.*, 2002), suggesting that the positioning of septins on the membrane proximal to FAs may facilitate MT growth trajectories into the nearby adhesion. Thus, our experimental photoactivation of Rac1 may locally drive enhanced membrane curvature that is sufficient to position peripheral septins adjacent to FAs, potentially mimicking a scenario that is normally controlled through the combined efforts of FA-associated actomyosin and Rac1 signaling.

While it is clear that peripheral FA-associated septins display a preference for NC MTs, it remains unclear how or why septins distinguish NC MTs from centrosomal MTs. Experimental evidence shows that septin oligomeric complexes interact with MT plus ends and compete for EB1 binding in a GTP-dependent manner (Nakos *et al.*, 2019); however, there is no evidence that NC MTs are structurally distinct from centrosomal MTs in tubulin composition or affinity for end-binding proteins. One possible mechanism for septin targeting of NC MTs may be through differential posttranslational modifications of NC MTs, as there is strong evidence that septins recognize and bind preferentially to polyglutamylated tubulin, which drives polarized epithelial cell morphologies (Spiliotis *et al.*, 2008) and results in enhanced stabilization of polyglutamylated MTs (Targa *et al.*, 2019). Thus, while this study has identified at least one functional role for septins and NC MTs, future studies are needed to determine how cells designate and coordinate functionally distinct contributions of centrosomal and NC MTs.

MATERIALS AND METHODS

[Request a protocol](#) through [Bio-protocol](#).

Cell culture and drug treatments

Human umbilical vein endothelial cells (HUVECs) were cultured in EC basal medium (EBM) supplemented with growth supplements (Cell Applications) and penicillin–streptomycin (Fisher) and maintained at 37°C in 5% CO₂. All transfections were performed in Mirus Nucleofection buffer using a Lonza Nucleofector Device, setting A-034. ECs were cultured at 75,000–100,000 cells/coverslip and plated on 10 µg/ml fibronectin-coated 35 mm glass bottom dishes (Cat. #: P35G-1.0-20-C.s). Transfections were imaged 3 h after experimental cDNA transfections unless indicated otherwise (for MT group prep, see below). For nocodazole experiments, cells were treated with 10 µM nocodazole for 20 min and washed out with EBM before imaging. Cells treated with s-nitro blebbistatin (20 µM; Cayman Chemicals) in dimethyl sulfoxide (DMSO; 0.001%) were monitored every 20 min for 60 min before being imaged at 60 min. Blebbistatin washout experiments were done with >6 EBM changes. Latrunculin experiments were done at 1.25 µM resuspended in DMSO; 0.001%. Cells were treated on the microscope stage and imaged immediately after.

NC and centrosomal cell prep

HUVECs were incubated in 1.2 µM centrinone (Plk4 inhibitor that prevents centriole duplication and leads to centrosome depletion; Wong *et al.*, 2015) for 9 d before use. Media was changed or cells split every 2–3 d, consistent with normal HUVEC handling. For NC cell prep, cells were transfected with pCMV2-FLAG-CDK5RAP2 F75A (51–100) (a gift from R. Qi, Hong Kong University of Science and Technology; Choi *et al.*, 2010; Sanders *et al.*, 2017). Cells were allowed to express the γ-TuNA inhibitor for 24 h before imaging to ensure full Golgi-derived MT KD.

Live-cell imaging

All imaging was performed on a spinning disk (Yokogawa CSU-X1; Andor Technology) confocal microscope using a 60 × 1.4 NA oil immersion objective lens on a TiE microscope equipped with a Perfect Focus System (Nikon) equipped with an electronic shutter (Smart shutter; Sutter Instrument) for transmitted illumination, a linear encoded X and Y, motorized stage (ASI Technologies), and a multibandpass dichromatic mirror (Semrock) and bandpass filters (Chroma Technology Corp.) in an electronic filter wheel for selection of GFP or Texas red emission. Laser illumination (561- and 488-nm) was provided by a custom-built laser combiner module (modification of LMM-3; Spectral Applied Research) containing 500-mW solid state lasers (488 nm [Coherent] and 561 nm [MPB Communications]) that were shuttered with electronic shutters and attenuated and/or directed to a fiber-coupled output port with an Acousto optic tunable filter (Neos Technologies) and directed to the confocal scan-head via a single-mode optical fiber (Oz Optics). Time-lapse videos were acquired using a Coolsnap HQ2 cooled charge-coupled device camera (Photometrics) or a Clara cooled charge-coupled device camera (Andor Technology) operated in the 14-bit mode for 3 min at 3-s image intervals using a 300–400-ms exposure time. Microscope system automation was controlled with Metamorph software (Molecular Devices) or NIS Elements software (Nikon). Images of BFP-labeled constructs were taken using epifluorescent illumination with a filter set (ex/em 405/510) and exposure times of 800 ms. After acquisition, general image processing involved optimization of image brightness and contrast using the acquisition software package. Additional microscopy image manipulations and measurements are described in detail in the appropriate *Materials and Methods* subsections.

Cell migration assay

Cell migration assays were performed on fibronectin-coated coverslips (previously described), but with the following modifications. Before plating the cells, the fibronectin-coated coverslips were dried using an aspirator. Transfected HUVECs (500,000–750,000) were then cultured in 50 µl of EBM on the center of the dried coverslip to concentrate the cells and were allowed to adhere to the coverslip and form a confluent monolayer. The monolayer was then rinsed with EBM to remove unattached cells and scraped with a razor blade to generate a wound edge. Images were collected on an EVOS microscope under 10× or 20×. All data were measured under 10× at consistent intervals over the course of 2 d (Cory, 2011). Wound closure speed is reported as distance traveled/time elapsed.

MT dynamics analysis

MT dynamics were analyzed from EB3 videos using plusTipTracker software (Applegate *et al.*, 2011), a Matlab-based, open-source software package that combines automated detection, tracking, analysis, and visualization tools for movies of fluorescently labeled MT plus end binding proteins (+TIPs). The +TIP comet detection algorithm relies on a watershed-based approach to estimate locally optimal thresholds. The track reconstruction algorithm uses the spatially and temporally globally optimized tracking framework described in Jaqaman *et al.* (2008), with cost functions modified to reflect MT track geometry. In brief, tracking occurs in two steps: frame-to-frame linking of comets into growth subtracks and the linking of collinear, sequential growth subtracks into compound tracks. The cost of joining two candidate growth subtracks into a compound track is calculated from three spatial parameters and one temporal parameter. After calculating the cost of linking all pairs of candidate growth tracks, the links are chosen by minimizing the global cost, which is achieved by solving the Linear Assignment Problem (Jaqaman *et al.*, 2008).

Tracking parameters

Tracking control parameters were optimized based on a parameter sweep using the plusTipParamSweepGUI tool of plusTipTracker (Applegate *et al.*, 2011) and verified by visual inspection of track overlays on movies. The same parameter set was used for all movies in the data set: maximum gap length, 12 frames; minimum track length, three frames; search radius range, 5–10 pixels; maximum forward angle, 25°; maximum backward angle, 8°; maximum shrinkage factor, 1.0; fluctuation radius, 2 pixels. For this study, only growth excursions were of interest, so MT shrinkage or pause events were not analyzed. However, subtrack linking was still performed to correct for the many occurrences when comets cross over one another or disappear momentarily from the field of view by focal drift, which breaks the trajectories prematurely.

MT count and FA size relative to MT count

The MT count was taken directly from plusTipTracker data. The FA size relative to the MT count was calculated by standardizing MT counts to the lowest value and multiplying existing FA size data for groups by the calculated coefficient.

Expression constructs

cDNAs, labeled with GFP (CLASP1, EB3, MCAK), mApple (EB3, F-Tractin), or BFP (paxillin, MCAK, EB3), were generated by the Michael Davidson lab (Florida State University) and provided by the Clare Waterman lab (National Institutes of Health/National Heart, Lung, and Blood Institute, Bethesda, MD). GFP-CAMSAP2

was provided by the lab of Anna Akhmanova of Utrecht University in the Netherlands. Septin 2, 6, and 7 constructs were provided by E. S. All cDNA used for transfection was prepared using the Plasmid Mini or Maxi kit (Qiagen). EGFP–Aurora-A was obtained from E. Nigg (University of Basel, Basel, Switzerland) and modified as follows. The Em–Aurora-A fusion was assembled using an advanced EGFP variant with several mutations designed to enhance brightness and folding efficiency (Em: wild-type GFP + F64L, S65T, S72A, N149K, M153T, I167T, and A206K; Teerawanichpan *et al.*, 2007). The resulting targeting vectors were used as pilots to demonstrate proper localization of the fusions to their designated subcellular locations. Nonphosphorylatable (serine to alanine) and phosphomimic (serine to glutamic acid) MCAK constructs were mutated in multiple known Aurora phosphorylation sites (serines 92, 106, 108, 112, and 196 [AAAAA MCAK and EEEEE MCAK]; Braun *et al.*, 2014).

MT dynamics analysis

MT dynamics were analyzed from fluorescently labeled EB3 (GFP-EB3) movies using plusTipTracker software, a MATLAB-based, open-source software package that combines automated detection, tracking, analysis, and visualization tools for movies of fluorescently labeled MT plus end binding proteins as previously described (Jaqaman *et al.*, 2008; Applegate *et al.*, 2011; Myers *et al.*, 2011; Braun *et al.*, 2014; D'Angelo *et al.*, 2017). All MT growth parameter tracking was performed three times.

Statistical analysis

MT growth tracks were pooled per cell, and the average growth speeds and lifetimes from each cell were taken collectively as one event for each experimental group (n = number of cells). All MT dynamics data were collected from three separate experiments and are displayed as mean \pm SEM. One-way analysis of variance tests with post-hoc Student's *t* test analysis was performed to determine statistical significance between cells within each experimental group and between each experimental group separately for MT growth speed and MT growth lifetime. For statistical significance, α was set to 0.05, yielding a 95% confidence level.

Plasmids for purification

The plasmid encoding His-SEPT2-mCherry (pET15b—His-SEPT2-mCherry) was a gift from Shae Padrick (College of Medicine, Drexel University). The plasmid encoding SEPT6/7-strep (pnCS—SEPT6/7-strep; Amy Gladfelter, Department of Biology, University of North Carolina) with the additional 19 amino acids at the N-terminal of SEPT7 was constructed as before (Nakos *et al.*, 2019).

Protein expression and purification

The recombinant mCherry-SEPT2/6/7 complex was expressed and purified as described before (Mavrakis *et al.*, 2014; Nakos *et al.*, 2019). mCherry-SEPT2/6/7 was dialyzed overnight at 4°C in BRB20 (20 mM PIPES, pH 6.9, 2 mM MgCl₂, 1 mM EGTA [ethylene glycol-bis(2-aminoethylether)-*N,N,N',N'*-tetraacetic acid]).

The recombinant mCherry-SEPT2/6/7 complex was expressed in *Escherichia coli* BL21 (DE3) cells (Invitrogen) cotransformed with plasmids encoding His-SEPT2-mCherry and SEPT6/7-strep, as described (Mavrakis *et al.*, 2014; Nakos *et al.*, 2019). Bacterial cells were grown at 37°C until OD₆₀₀ of 0.5 and subsequently induced with 0.2 mM isopropyl β -*D*-1-thiogalactopyranoside (IPTG) for 16 h at 18°C. Bacterial cells were centrifuged at 4000 rpm for 20 min at 4°C, and the resultant cell pellets were resuspended in lysis buffer (50 mM Tris-HCl, pH 8.0, 500 mM KCl, 10 mM imidazole, 5 mM

MgCl₂, 1 mg/ml lysozyme, 1 mM phenylmethylsulfonyl fluoride [PMSF], and 1 \times Bacterial Protease Arrest cocktail [G-Biosciences; 786–330]). Cells were lysed by sonication (10 sets of 15 pulses on ice with a 30-s interval between each set), and cell lysates were centrifuged at 13,000 rpm for 30 min at 4°C. Supernatants were passed through a 0.45- μ m-pore filter and loaded onto gravity flow columns with Ni-NTA agarose beads (745400.25; Macherey-Nagel) equilibrated with binding buffer (50 mM Tris-HCl, pH 8.0, 500 mM KCl, 10 mM imidazole, 5 mM MgCl₂, 1 mM PMSF, and 1 \times Bacterial Protease Arrest cocktail). Proteins were eluted from Ni-NTA columns with elution buffer (50 mM Tris-HCl, pH 8.0, 500 mM KCl, 250 mM imidazole, and 5 mM MgCl₂) and subsequently loaded to a Strep-Trap HP column (GE Healthcare) equilibrated with 50 mM Tris-HCl, pH 8.0, 300 mM KCl, and 5 mM MgCl₂. Proteins were eluted from the Strep column with elution buffer (50 mM Tris-HCl, pH 8.0, 300 mM KCl, 5 mM MgCl₂, and 2.5 mM *D*-desthiobiotin [Sigma; D1411]) and dialyzed overnight at 4°C in BRB20 (20 mM PIPES, pH 6.9, 2 mM MgCl₂, 1 mM EGTA). Recombinant mCherry-SEPT2/6/7 was further purified using an AKTA FPLC system (GE Healthcare) with a Superdex 200 10/300 GL (Amersham Biosciences) gel filtration column.

Purified GFP-MCAK

Purified GFP-MCAK was provided by the lab of Claire Walczak with help from Stephanie Ems-McClung from Indiana University. It was provided at 3.75 μ M in 409 mM KCl, 20 mM PIPES, pH 6.8, 1 mM MgCl₂, 1 mM EGTA, 0.1 mM EDTA, 1 mM dithiothreitol, 10 μ M MgATP, 10% sucrose.

In vitro TIRF MT depolymerization assays

Imaging total internal reflection fluorescence (TIRF) chambers were prepared as described before (Tanenbaum *et al.*, 2013; Reid *et al.*, 2016; Nakos *et al.*, 2019). For depolymerization assays, imaging chambers were treated sequentially with 1% pluronic F-127 for 5 min, 5 mg/ml biotin–bovine serum albumin (BSA) (A8549; Sigma-Aldrich) for 5 min, 0.5 mg/ml Neutravidin (A2666; Invitrogen) for 5 min and blocking buffer (BRB80, 1% pluronic F-127, 1 mg/ml BSA) for 5 min. Imaging chambers were washed with BRB80–1 mg/ml BSA and incubated with GMPCPP-stabilized HiLyte-647–labeled MTs diluted in BRB80–1 mg/ml BSA for 15 min. GMPCPP-stabilized MTs were prepared by incubating 20 μ M tubulin containing 77% unlabeled tubulin (T240; Cytoskeleton) with 11.5% biotin–tubulin (T333P; Cytoskeleton) and 11.5% HiLyte-647-tubulin (TL670M; Cytoskeleton) with 1 mM GMPCPP (NU-405L; Jena Bioscience) in BRB80 (80 mM PIPES, pH 6.9, 2 mM MgCl₂, 1 mM EGTA) at 37°C for 30 min. MTs were diluted in BRB80 and spun for 15 min at 100,000 $\times g$ (Optima TL100; Beckman Coulter). Sedimented MTs were resuspended in BRB80. Subsequently, imaging chambers were washed with BRB20–1 mg/ml BSA. MT depolymerization reactions were initiated by the addition of 1 nM GFP-MCAK in BRB20 supplemented with 1 mM ATP, 1 mg/ml BSA, 0.25% pluronic F-127, 0.1% κ -casein, 75 mM KCl, an oxygen scavenging system (0.5 mg/ml glucose oxidase, 0.1 mg/ml catalase, 4.5 mg/ml *D*-glucose, 70 mM β -mercaptoethanol), and recombinant mCherry-SEPT2/6/7. Imaging chambers were sealed with vacuum grease before imaging at room temperature. Imaging was performed every 2 s for 5 min.

In vitro TIRF microscopy assays were performed at Drexel University's Cell Imaging Center with the DeltaVision OMX V4 inverted microscope (GE Healthcare) equipped with a 60 \times /1.49 NA TIRF objective lens (Olympus), motorized stage, sCMOS pco.edge cameras (PCO), stage top incubator with temperature controller, and the softWoRx software.

FA size measurements

FA sizes were performed by measuring the length of the paxillin-labeled FA along its longest length. Fluorescence was adjusted so that the distal tips of each FA were clearly defined. Any significant drop of fluorescence value to that of cytosolic levels was defined as the edge of the FA to account for multiple FA accumulations within a region. Forty to sixty FAs were measured in each cell across four general areas of the cell to account for variations in FA accumulation due to potential ECM defects. Individual cells were held to a 95% confidence interval before an average was calculated. Within each group, each cell average was used to generate a subsequent 95% confidence interval to create an average of averages that are presented in the figures. Measurement was via Nikon NIS elements AR software measurement tools.

Statistical analyses

Statistical analyses were done with paired and unpaired *T* tests assuming equal variance between groups with a one-way analysis of variance assuming $\alpha < 0.05$. All data are presented as an average of averages; within cell measurements.

FA assembly and disassembly rate measurements

Time-lapse paxillin image processing and FA assembly and disassembly rates were calculated using the FA analysis server (FAAS) hosted by the lab of Shawn Gomez at the University of North Carolina at Chapel Hill (Berginski and Gomez, 2013). All movies analyzed were 60 min time-lapse images of paxillin-labeled FAs with images taken every 2 min.

CAMSAP2 stretch length and counts

CAMSAP2 stretch length was measured using FIJI software's segmented line and drawing a line through the main mass of the CAMSAP-labeled MT minus end (Tanaka *et al.*, 2012). Each measured stretch had clearly defined ends. Brightness/contrast was adjusted to lowest bounds to identify crossing signals of multiple stretches. More than 30 stretches were counted per $n > 14$ cells across each group. Data shown are average of averages held to 95% confidence intervals. CAMSAP counts were measured by identifying each unique stretch within a cell. All stretches measure across $n > 14$ cells per group.

MT growth into FA

Cells were divided into four regions based on the nucleus. In each region, a $10 \times 10 \mu\text{m}$ square was placed such that >3 FAs but less than 50% of the region was covered. Regions were placed away from the cell periphery to prevent bias toward MTs interacting with membranes being mistaken for termination into FAs. All EB-labeled MTs that came inside 1 pixel from the region were counted as an event. MTs were counted across a 3-min time lapse, and the position of signal loss was recorded. Positive growth into FAs was loss of signal in the main mass of the paxillin-labeled FA. Those MTs that either did not leave the region or whose signal had not expired after the 3-min time lapse were disregarded. Twenty regions across >5 cells were measured and averaged for each condition. Frequency was determined by (MT growth into FA)/(total events). Graphs are standardized to control cells with both MT groups.

MT colocalization with septin

MT plus tips were considered colocalized with Septin 7 where the MT passed through the long axis of the Septin 7 within the same frame of a time lapse.

MT growth to FAs

MTs were tracked after the above interaction for the length of the time lapse. Those MTs whose signal terminated into the mass of the FA were considered (+), and those whose signal terminated anywhere else (-). Only MTs that could be fully tracked within the time lapse were considered. MT colocalization with Septin 7 was counted across $n > 10$ cells and presented as an average of averages. Frequencies calculated as (number of MTs landing at FAs)/(total septin-colocalized MTs) with $\times 100$ for percentages. MT colocalization and septin-associated MT growth into FAs are presented as standardized to centrosomal cells (centrosomal set to 1). Determination for average MT colocalization was done by counting every peripheral Septin 7 as identified by Septin 7 signals within 5 microns of the cell membrane or as 1.5 SD below the average pixel intensity of perinuclear Septin 7 signals if outside the perinuclear Septin 7 zone (5–7.5 microns from the nucleus) and not in the strictly peripheral Septin 7 region. All MT colocalizations with these peripheral septins were recorded and standardized to all MT tracks breaching four $10 \times 10 \mu\text{m}$ squares within cells throughout a 3-min time-lapse movie as described above. More than five cells were calculated as an average of averages with 95% confidence and represented as standardized to centrosomal cells.

Kymographs

Kymographs were created using the FIJI (FIJI is just ImageJ) software plug-in kymograph feature. Lines were drawn with an average width of 5 pixels and presented as the *y*-axis: time and *x*-axis: distance.

MT speed with and without septin colocalization

MT speed was measured using FIJI's manual tracking plug-in. Comets were identified and followed across time-lapse movies and separated into two groups, colocalized with septin or without colocalization with septin; colocalization with septin as described above. Before groups were measured until the frame wherein septin and MT signals were overlapped. After groups started at the last frame from the "Before" group and followed the MT until termination.

Photoactivatable-Rac1

Using fluorescence recovery after photobleaching (FRAP) at 405 nm, HUVECs were subjected to a 405 nm laser within given regions. Unlabeled photoactivatable-Rac1 (PA-Rac1) undergoes a reconfiguration to locally activate Rac1 within the FRAP region after two stimulations of 100 ns by the 405 nm laser (Wu *et al.*, 2009).

Photodissociation

π -EB1 constructs were generously provided by the lab of Torsten Wittmann and were used with communication from his graduate student Jeffrey Van Haren at the University of California San Francisco; π -EB1 consists of photo-sensitive EB1C and EB1N constructs whereby the EB1C is dissociated from the MT plus end in response to 488 nm laser exposure while the EB1N is retained on the MT plus end. Upon laser dissociation of EB1C (the MAP-binding domain of EB) all MAPs bound to the EB1C terminus also dissociate. EB1N-mScarlet1-LZ-LOV2, EB1N-LZ-LOV2 (no fluorescent tag), EB1N-LZ-LOV2F (fast variant of LOV2), mCherry-Zdk1-EB1C, 107696 GFP-Zdk1-EB1C (AddGene) as previously described (Van Haren *et al.*, 2018).

Max intensity overlays

Using NIS Elements AR software, max intensities were created using the Maximum image function with a relative range selection from:

First to +0 to run the expression function: "File Name".Maximum [First...+0]. The process creates a normal maximum intensity overlay image but for each subsequent frame of a time lapse, it stitches previous max intensities together to create a movie of normally static image processes.

Immunofluorescence

Fixation and processing of sample for immunofluorescence labeling was performed with either a paraformaldehyde/glutaraldehyde coextraction/fixation buffer (PFG-PHEM; 4% paraformaldehyde, 0.15% glutaraldehyde, 0.2% Triton X-100 in 60 mM Pipes, 27.3 mM HEPES, 10 mM EGTA, and 8.2 mM MgSO₄, pH 7.0; Supplemental Figure S1F) or a paraformaldehyde without glutaraldehyde fixation buffer (PF-PHEM; 4% paraformaldehyde, 27.3 mM HEPES, 10 mM EGTA, and 8.2 mM MgSO₄, pH 7.0; Supplemental Figure S1C) or ice-cold methanol (Supplemental Figure S1, D and E). Transfection protocol was followed as described above for expression constructs before fixation (Supplemental Figure S1C; Septin 7 and FAs). For PFG-PHEM, fixation buffer was added to HUVECs plated on fibronectin-coated coverslips at room temperature for 5 min, followed by rinsing (3–5 min) with 1× phosphate-buffered saline (PBS) (minus Ca²⁺ and Mg²⁺) treated with 0.01 g/ml NaBH₄ in 1× PBS (2 × 15 min) to quench reactive aldehydes. Cells were rinsed once with 1× PBS, and finally blocked with 5% BSA in 1× PBS (1 h at room temperature). Mouse anti- α -tubulin (EMD Millipore; DM1 α 1:2000) primary was incubated overnight at 4°C. Coverslips were then rinsed with PBS, blocked again with 5% BSA, and secondary stained with anti-mouse Cy5-conjugated immunoglobulin G (IgG) (Jackson ImmunoResearch Laboratories; 1:5000). Cells were washed with PBS and stained with phalloidin iFluor 405 for 45 min in 1% BSA in PBS. Coverslips were washed and then mounted with mounting medium (Dako) and imaged. For PF-PHEM, cells were treated as previously described but were not incubated with NaBH₄. Primary anti-Septin 2 (1:500), 6 (1:100), and 9 (1:200) antibodies (from the lab of E. S.) were incubated with anti-Septin 7 (ImmunoBiological Laboratories; 1:500). Secondary staining was performed with corresponding Cy2-, Cy3-, or Cy5-conjugated IgG (Jackson ImmunoResearch Laboratories; 1:500) or Alexa Fluor 405 (ThermoFisher; 1:250). For methanol fixation, cells were primary stained with mouse anti- α -tubulin (described above) and rabbit anti-Septin 7 (ImmunoBiological Laboratories; 1:2500). Secondary staining performed with anti-mouse or anti-rabbit IgG Cy3- or Cy5-conjugated igG (Jackson ImmunoResearch Laboratories; DM1 α 1:5000; Septin 7: 1:1000). Cells were washed and either incubated with phalloidin as described above or restained with rabbit anti-Septin 6 (from the lab of E. S.; 1:500) primary and Cy2 secondary (anti-rabbit; Jackson ImmunoResearch Laboratories; 1:1000).

Western blotting

Cytoplasmic extracts from HUVECs were isolated in NP-40 lysis buffer (50 mM Tris, pH 8.0, 150 mM NaCl, 0.5% 1 M NaF, and 1% Triton X-100 with Halt Protease Inhibitor Cocktail [Thermo Scientific]). Protein from supernatants were quantified with the Pearson 660 method. Proteins (15 μ g) were mixed with Laemmli sample buffer and separated by SDS-PAGE. After electrophoresis, proteins were electrotransferred to a polyvinylidene fluoride (PVDF) transfer membrane. For protein detection, membranes were blocked for 2 h at room temperature with 5% milk, 1% BSA in TBST buffer (20 mM Tris, pH 7.6, 137 mM NaCl₂, and 0.1% Tween-20) and incubated overnight at 4°C with mouse GAPDH (1:2000; Abcam) and Septin 7 (ImmunoBiological Laboratories; 1:1500). After primary antibody

incubation, blots were washed five times with TBST (3 min each) and incubated with IRDye 680 goat anti-mouse (LI-COR; 1:20,000) and IRDye 800 goat anti-rabbit (LI-COR; 1:20,000). Blots were imaged using the Li-COR Odyssey CLx imaging system. Densitometry of Western blots was performed using ImageJ software. Values were standardized to GAPDH values.

siRNA oligonucleotides

CLASP1-siRNA custom sequence: 5' GGGUAAUACUGACGAGCUUU 3' was previously verified (Dharmacon; Myer and Myers, 2017). Septin 7 siRNA isoform 5 sequence: 5' GAAGCUCAACAACGUUUU 3'; Septin 7 siRNA isoform 6 sequence: 5' UGAAUUCACGCUUAUGGUA 3'; Septin 7 siRNA isoform 7 sequence: 5' GGGGAAGAUUUUAAA-CUC 3'; and Septin 7 siRNA isoform 8 sequence: 5' UAUGAGAACU-ACAGAAGCA 3' were purchased from Dharmacon/Horizon Discovery; nontargeting siRNA sequence: 5' UGGUUUACAUGUCGACUAA 3' from Dharmacon/Horizon Discovery. HUVECs were transfected with siRNA 24 h before lysate collection for Western blotting and for fluorescence live-cell imaging.

Video generation

Video brightness and contrast were adjusted in Nikon NIS Elements AR software and exported as .mov or .avi files. Adobe Premiere Pro software (San Jose, CA) was used to insert text labels, timers, graphics, and scale bars, and video files were then exported as .mp4 files with H.264 formatting at 1080p HD and maximum render quality.

ACKNOWLEDGMENTS

We thank Claire Walczak and Stephanie Ems-McClung for providing purified GFP-MCAK used for in vitro microtubule assays, Torsten Wittmann for providing the π -EB1 photo-dissociation constructs, Angelica Patel for assistance with migration analysis, and all members of the Myers laboratory for critical analysis and helpful discussion. This work was supported by a National Institute of General Medical Sciences (NIGMS) Academic Research Enhancement Award (grant number 1R15GM139063-01; to K.A.M.) and a NIGMS R35 Award (1R35 GM136337-01; to E.T.S.). D.M., T.P., S.J.D., A.G., and P.P. were supported by the Department of Biological Sciences, University of the Sciences. K.N. was supported by NIGMS R35 Award (1R35 GM136337-01).

REFERENCES

- Aher A, Kok M, Sharma A, Rai A, Olieric N, Rodriguez-Garcia R, Katrukha EA, Weinert T, Olieric V, Kapitein LC, et al. (2018). CLASP suppresses microtubule catastrophes through a single TOG domain. *Dev Cell* 46, 40–58.e48.
- Akhmanova A, Hoogenraad CC (2015). Microtubule minus-end-targeting proteins. *Curr Biol* 25, R162–R171.
- Akhmanova A, Steinmetz MO (2010). Microtubule +TIPs at a glance. *J Cell Sci* 123, 3415–3419.
- Aoki K, Nakamura T, Matsuda M (2004). Spatio-temporal regulation of Rac1 and Cdc42 activity during nerve growth factor-induced neurite outgrowth in PC12 cells. *J Biol Chem* 279, 713–719.
- Applegate KT, Besson S, Matov A, Bagonis MH, Jaqaman K, Danuser G (2011). plusTipTracker: quantitative image analysis software for the measurement of microtubule dynamics. *J Struct Biol* 176, 168–184.
- Ashley TM, Benjamin DR, Yampolsky D, Michael TS, Straube A, Hayashi I, Kaverina I (2014). CLASPs are required for proper microtubule localization of end-binding proteins. *Dev Cell* 30, 343–352.
- Bai X, Karasmanis EP, Spiliotis ET (2016). Septin 9 interacts with kinesin KIF17 and interferes with the mechanism of NMDA receptor cargo binding and transport. *Mol Biol Cell* 27, 897–906.
- Beber A, Alqabandi M, Prevost C, Viars F, Levy D, Bassereau P, Bertin A, Mangenot S (2019). Septin-based readout of PI(4,5)P₂ incorporation into membranes of giant unilamellar vesicles. *Cytoskeleton (Hoboken)* 76, 92–103.

- Berginski ME, Gomez SM (2013). The focal adhesion analysis server: a web tool for analyzing focal adhesion dynamics. *F1000Research* 2, 68.
- Bhadriraju K, Yang M, Alom Ruiz S, Pirone D, Tan J, Chen CS (2007). Activation of ROCK by RhoA is regulated by cell adhesion, shape, and cytoskeletal tension. *Exp Cell Res* 313, 3616–3623.
- Blanco C, Morales D, Mogollones I, Vergara-Jaque A, Vargas C, Álvarez A, Riquelme D, Leiva-Salcedo E, González W, Morales D, et al. (2019). EB1- and EB2-dependent anterograde trafficking of TRPM4 regulates focal adhesion turnover and cell invasion. *FASEB J* 33, 9434–9452.
- Bowen JR, Hwang D, Bai X, Roy D, Spiliotis ET (2011). Septin GTPases spatially guide microtubule organization and plus end dynamics in polarizing epithelia. *J Cell Biol* 194, 187–197.
- Braun A, Dang K, Buslig F, Baird MA, Davidson MW, Waterman CM, Myers KA (2014). Rac1 and Aurora A regulate MCAK to polarize microtubule growth in migrating endothelial cells. *J Cell Biol* 206, 97–112.
- Bridges AA, Jentsch MS, Oakes PW, Occhipinti P, Gladfelter AS (2016). Micron-scale plasma membrane curvature is recognized by the septin cytoskeleton. *J Cell Biol* 213, 23–32.
- Broussard JA, Webb DJ, Kaverina I (2008). Asymmetric focal adhesion disassembly in motile cells. *Curr Opin Cell Biol* 20, 85–90.
- Cannon KS, Woods BL, Crutchley JM, Gladfelter AS (2019). An amphipathic helix enables septins to sense micrometer-scale membrane curvature. *J Cell Biol* 218, 1128–1137.
- Choi Y-K, Liu P, Sze SK, Dai C, Qi RZ (2010). CDK5RAP2 stimulates microtubule nucleation by the γ -tubulin ring complex. *J Cell Biol* 191, 1089–1095.
- Cory G (2011). Scratch-wound assay. *Methods Mol Biol* 769, 25–30.
- D'Angelo L, Myer NM, Myers KA (2017). MCAK-mediated regulation of endothelial cell microtubule dynamics is mechanosensitive to myosin-II contractility. *Mol Biol Cell* 28, 1223–1237.
- Dolat L, Hunyara JL, Bowen JR, Karasmanis EP, Elgawly M, Galkin VE, Spiliotis ET (2014). Septins promote stress fiber-mediated maturation of focal adhesions and renal epithelial motility. *J Cell Biol* 207, 225–235.
- Efimov A, Kaverina I (2009). Significance of microtubule catastrophes at focal adhesion sites. *Cell Adh Migr* 3, 285–287.
- Efimov A, Schiefermeier N, Grigoriev I, Ohi R, Brown MC, Turner CE, Small JV, Kaverina I (2008). Paxillin-dependent stimulation of microtubule catastrophes at focal adhesion sites. *J Cell Sci* 121, 196–204.
- Ezraty EJ, Bertaux C, Marcantonio EE, Gundersen GG (2009). Clathrin mediates integrin endocytosis for focal adhesion disassembly in migrating cells. *J Cell Biol* 187, 733–747.
- Ezraty EJ, Partridge MA, Gundersen GG (2005). Microtubule-induced focal adhesion disassembly is mediated by dynamin and focal adhesion kinase. *Nat Cell Biol* 7, 581–590.
- Folkman J (1995). Angiogenesis in cancer, vascular, rheumatoid and other disease. *Nat Med* 1, 27–31.
- Gardel ML, Schneider IC, Aratyn-Schaus Y, Waterman CM (2010). Mechanical integration of actin and adhesion dynamics in cell migration. *Annu Rev Cell Dev Biol* 26, 315–333.
- Gouveia SM, Akhmanova A (2010). Cell and molecular biology of microtubule plus end tracking proteins: end binding proteins and their partners. *Int Rev Cell Mol Biol* 285, 1–74.
- Grabham PW (2003). Microtubule and Rac 1-dependent F-actin in growth cones. *J Cell Sci* 116, 3739–3748.
- Jaqaman K, Loerke D, Mettlen M, Kuwata H, Grinstein S, Schmid SL, Danuser G (2008). Robust single-particle tracking in live-cell time-lapse sequences. *Nat Methods* 5, 695–702.
- Kaverina I, Krylyshkina O, Small JV (1999). Microtubule targeting of substrate contacts promotes their relaxation and dissociation. *J Cell Biol* 146, 1033–1044.
- Kaverina I, Rottner K, Small JV (1998). Targeting, capture, and stabilization of microtubules at early focal adhesions. *J Cell Biol* 142, 181–190.
- Kremer BE, Haystead T, Macara IG (2005). Mammalian septins regulate microtubule stability through interaction with the microtubule-binding protein MAP4. *Mol Biol Cell* 16, 4648–4659.
- Krylyshkina O, Kaverina I, Kranewitter W, Steffen W, Alonso MC, Cross RA, Small JV (2002). Modulation of substrate adhesion dynamics via microtubule targeting requires kinesin-1. *J Cell Biol* 156, 349–360.
- Kumar P, Lyle KS, Gierke S, Matov A, Danuser G, Wittmann T (2009). GSK3 β phosphorylation modulates CLASP-microtubule association and lamella microtubule attachment. *J Cell Biol* 184, 895–908.
- Lawson CD, Burridge K (2014). The on-off relationship of Rho and Rac during integrin-mediated adhesion and cell migration. *Small GTPases* 5, e27958.
- Lee T, Langford KJ, Askham JM, Brüning-Richardson A, Morrison EE (2008). MCAK associates with EB1. *Oncogene* 27, 2494–2500.
- Lim BC, Matsumoto S, Yamamoto H, Mizuno H, Kikuta J, Ishii M, Kikuchi A (2016). Prickle1 promotes focal adhesion disassembly in cooperation with the CLASP-LL5 β complex in migrating cells. *J Cell Sci* 129, 3115–3129.
- Limouze J, Straight AF, Mitchison T, Sellers JR (2004). Specificity of blebbistatin, an inhibitor of myosin II. *J Muscle Res Cell Motil* 25, 337–341.
- Liu BP, Chrzanoska-Wodnicka M, Burridge K (1998). Microtubule depolymerization induces stress fibers, focal adhesions, and DNA synthesis via the GTP-binding protein rho. *Cell Adhes Commun* 5, 249–255.
- Lorenzo C, Liao Q, Hardwicke MA, Ducommun B (2009). Pharmacological inhibition of Aurora-A but not Aurora-B impairs interphase microtubule dynamics. *Cell Cycle* 8, 1733–1737.
- Martin M, Veloso A, Wu J, Katrukha EA, Akhmanova A (2018). Control of endothelial cell polarity and sprouting angiogenesis by non-centrosomal microtubules. *eLife* 7, e33864.
- Marvin LM, Babet MG, Akhmanova A, René (2011). A complex of Kif18b and MCAK promotes microtubule depolymerization and is negatively regulated by aurora kinases. *Curr Biol* 21, 1356–1365.
- Matsumoto S, Fumoto K, Okamoto T, Kaibuchi K, Kikuchi A (2010). Binding of APC and dishevelled mediates Wnt5a-regulated focal adhesion dynamics in migrating cells. *EMBO J* 29, 1192–1204.
- Mavrakis M, Azou-Gros Y, Tsai F-C, Alvarado J, Bertin A, Iv F, Kress A, Brasselet S, Koenderink GH, Lecuit T (2014). Septins promote F-actin ring formation by crosslinking actin filaments into curved bundles. *Nat Cell Biol* 16, 322–334.
- Mennella V, Rogers GC, Rogers SL, Buster DW, Vale RD, Sharp DJ (2005). Functionally distinct kinesin-13 family members cooperate to regulate microtubule dynamics during interphase. *Nat Cell Biol* 7, 235–245.
- Miller PM, Folkmann AW, Maia ARR, Efimova N, Efimov A, Kaverina I (2009). Golgi-derived CLASP-dependent microtubules control Golgi organization and polarized trafficking in motile cells. *Nat Cell Biol* 11, 1069–1080.
- Mimori-Kiyosue Y, Grigoriev I, Lansbergen G, Sasaki H, Matsui C, Severin F, Galjart N, Grosveld F, Vorobjev I, Tsukita S, Akhmanova A (2005). CLASP1 and CLASP2 bind to EB1 and regulate microtubule plus-end dynamics at the cell cortex. *J Cell Biol* 168, 141–153.
- Moon HH, Kreis NN, Friemel A, Roth S, Schulte D, Solbach C, Louwen F, Yuan J, Ritter A (2021). Mitotic centromere-associated kinesin (MCAK/KIF2c) regulates cell migration and invasion by modulating microtubule dynamics and focal adhesion turnover. *Cancers (Basel)* 13, 5673.
- Mostowy S, Cossart P (2012). Septins: the fourth component of the cytoskeleton. *Nat Rev Mol Cell Biol* 13, 183–194.
- Myer NM, Myers KA (2017). CLASP1 regulates endothelial cell branching morphology and directed migration. *Biol Open* 6, 1502–1515.
- Myers KA, Applegate KT, Danuser G, Fischer RS, Waterman CM (2011). Distinct ECM mechanosensing pathways regulate microtubule dynamics to control endothelial cell branching morphogenesis. *J Cell Biol* 192, 321–334.
- Nakos K, Radler MR, Spiliotis ET (2019). Septin 2/6/7 complexes tune microtubule plus end growth and EB1 binding in a concentration- and filament-dependent manner. *Mol Biol Cell* 30, 2913–2928.
- Nobes CD, Hall A (1999). Rho GTPases control polarity, protrusion, and adhesion during cell movement. *J Cell Biol* 144, 1235–1244.
- Nölke T, Schwan C, Lehmann F, Østevold K, Pertz O, Aktories K (2016). Septins guide microtubule protrusions induced by actin-depolymerizing toxins like Clostridium difficile transferase (CDT). *Proc Natl Acad Sci USA* 113, 7870–7875.
- Novak IL, Slepchenko BM, Mogilner A, Loew LM (2004). Cooperativity between cell contractility and adhesion. *Phys Rev Lett* 93, 268109.
- Parsons JT, Horwitz AR, Schwartz MA (2010). Cell adhesion: integrating cytoskeletal dynamics and cellular tension. *Nat Rev Mol Cell Biol* 11, 633–643.
- Rafael DM, Martin K, Reimann A, Pontelli V, Pertz O (2015). SrGAP2-dependent integration of membrane geometry and slit-robo-repulsive cues regulates fibroblast contact inhibition of locomotion. *Dev Cell* 35, 78–92.
- Rafiq NBM, Nishimura Y, Plotnikov SV, Thiagarajan V, Zhang Z, Shi S, Natarajan M, Viasnoff V, Kanchanawong P, Jones GE, Bershadsky AD (2019). A mechano-signalling network linking microtubules, myosin IIA filaments and integrin-based adhesions. *Nat Mater* 18, 638–649.
- Rannou Y, Troade M-B, Petretti C, Hans F, Dutertre S, Dimitrov S, Prigent C (2008). Localization of Aurora A and Aurora B kinases during interphase: role of the N-terminal domain. *Cell Cycle* 7, 3012–3020.
- Reid TA, Schuster BM, Mann BJ, Balchand SK, Plooster M, McClellan M, Coombes CE, Wadsworth P, Gardner MK (2016). Suppression of

- microtubule assembly kinetics by the mitotic protein TPX2. *J Cell Sci* 129, 1319–1328.
- Ridley AJ (2003). Cell migration: integrating signals from front to back. *Science* 302, 1704–1709.
- Risau W (1997). Mechanisms of angiogenesis. *Nature* 386, 671–674.
- Rong Y, Yang W, Hao H, Wang W, Lin S, Shi P, Huang Y, Li B, Sun Y, Liu Z, Wu C (2021). The Golgi microtubules regulate single cell durotaxis. *EMBO Rep* 22, e51094.
- Rooney C, White G, Nazgiewicz A, Woodcock SA, Anderson KI, Ballestrem C, Malliri A (2010). The Rac activator STEF (Tiam2) regulates cell migration by microtubule-mediated focal adhesion disassembly. *EMBO Rep* 11, 292–298.
- Saaristo A, Karpanen T, Alitalo K (2000). Mechanisms of angiogenesis and their use in the inhibition of tumor growth and metastasis. *Oncogene* 19, 6122–6129.
- Sanders AAWM, Chang K, Zhu X, Thoppil RJ, Holmes WR, Kaverina I (2017). Nonrandom γ -TuNA-dependent spatial pattern of microtubule nucleation at the Golgi. *Mol Biol Cell* 28, 3181–3192.
- Schnelzer A, Prechtel D, Knaus U, Dehne K, Gerhard M, Graeff H, Harbeck N, Schmitt M, Lengyel E (2000). Rac1 in human breast cancer: over-expression, mutation analysis, and characterization of a new isoform, Rac1b. *Oncogene* 19, 3013–3020.
- Seetharaman S, Etienne-Manneville S (2019). Microtubules at focal adhesions—a double-edged sword. *J Cell Sci* 132, jcs232843.
- Smith C, Dolat L, Angelis D, Forgacs E, Spiliotis ET, Galkin VE (2015). Septin 9 exhibits polymorphic binding to F-actin and inhibits myosin and cofilin activity. *J Mol Biol* 427, 3273–3284.
- Spiliotis ET, Hunt SJ, Hu Q, Kinoshita M, Nelson WJ (2008). Epithelial polarity requires septin coupling of vesicle transport to polyglutamylated microtubules. *J Cell Biol* 180, 295–303.
- Spiliotis ET, McMurray MA (2020). Masters of asymmetry—lessons and perspectives from 50 years of septins. *Mol Biol Cell* 31, 2289–2297.
- Stehbens SJ, Paszek M, Pemble H, Ettinger A, Gierke S, Wittmann T (2014). CLASPs link focal-adhesion-associated microtubule capture to localized exocytosis and adhesion site turnover. *Nat Cell Biol* 16, 558–570.
- Tanaka N, Meng W, Nagae S, Takeichi M (2012). Nezh/CAMSAP3 and CAMSAP2 cooperate in epithelial-specific organization of noncentrosomal microtubules. *Proc Natl Acad Sci USA* 109, 20029–20034.
- Tanenbaum ME, Vale RD, McKenney RJ (2013). Cytoplasmic dynein cross-links and slides anti-parallel microtubules using its two motor domains. *eLife* 2, e00943.
- Targa B, Klipfel L, Cantaloube I, Salameh J, Benoit B, Poüs C, Baillet A (2019). Septin filament coalignment with microtubules depends on SEPT9_i1 and tubulin polyglutamylation, and is an early feature of acquired cell resistance to paclitaxel. *Cell Death Dis* 10, 54.
- Teerawanichpan P, Hoffman T, Ashe P, Datla R, Selvaraj G (2007). Investigations of combinations of mutations in the jellyfish green fluorescent protein (GFP) that afford brighter fluorescence, and use of a version (VisGreen) in plant, bacterial, and animal cells. *Biochim Biophys Acta* 1770, 1360–1368.
- Van Aelst L, D'Souza-Schorey C (1997). Rho GTPases and signaling networks. *Genes Dev* 11, 2295–2322.
- Van De Willige D, Hoogenraad CC, Akhmanova A (2016). Microtubule plus-end tracking proteins in neuronal development. *Cell Mol Life Sci* 73, 2053–2077.
- Van Haren J, Charafeddine RA, Ettinger A, Wang H, Hahn KM, Wittmann T (2018). Local control of intracellular microtubule dynamics by EB1 photodissociation. *Nat Cell Biol* 20, 252–261.
- Vicente-Manzanares M, Ma X, Adelstein RS, Horwitz AR (2009). Non-muscle myosin II takes centre stage in cell adhesion and migration. *Nat Rev Mol Cell Biol* 10, 778–790.
- Waterman-Storer CM, Salmon E (1999). Positive feedback interactions between microtubule and actin dynamics during cell motility. *Curr Opin Cell Biol* 11, 61–67.
- Waterman-Storer CM, WorthyLake RA, Liu BP, Burrigge K, Salmon ED (1999). Microtubule growth activates Rac1 to promote lamellipodial protrusion in fibroblasts. *Nat Cell Biol* 1, 45–50.
- Weems AD, Welf ES, Driscoll MK, Mazloom-Farsibaf H, Chang B-J, Weiss BG, Chi J, Dean KM, Fiolka R, Danuser G (2021). Blebs Promote Cell Survival by Assembling Oncogenic Signaling Hubs, *bioRxiv*, <https://doi.org/10.1101/2021.04.23.441200>.
- Wittmann T, Bokoch GM, Waterman-Storer CM (2003). Regulation of leading edge microtubule and actin dynamics downstream of Rac1. *J Cell Biol* 161, 845–851.
- Wittmann T, Waterman-Storer CM (2005). Spatial regulation of CLASP affinity for microtubules by Rac1 and GSK3beta in migrating epithelial cells. *J Cell Biol* 169, 929–939.
- Wojnacki J, Quassollo G, Marzolo M-P, Cáceres A (2014). Rho GTPases at the crossroad of signaling networks in mammals. *Small GTPases* 5, e28430.
- Wolfenson H, Bershadsky A, Henis YI, Geiger B (2011). Actomyosin-generated tension controls the molecular kinetics of focal adhesions. *J Cell Sci* 124, 1425–1432.
- Wong YL, Anzola JV, Davis RL, Yoon M, Motamedi A, Kroll A, Seo CP, Hsia JE, Kim SK, Mitchell JW, et al. (2015). Reversible centriole depletion with an inhibitor of Polo-like kinase 4. *Science* 348, 1155–1160.
- Woods BL, Gladfelter AS (2021). The state of the septin cytoskeleton from assembly to function. *Curr Opin Cell Biol* 68, 105–112.
- Wu J, Akhmanova A (2017). Microtubule-organizing centers. *Annu Rev Cell Dev Biol* 33, 51–75.
- Wu X, Kodama A, Fuchs E (2008). ACF7 regulates cytoskeletal-focal adhesion dynamics and migration and has ATPase activity. *Cell* 135, 137–148.
- Wu YI, Frey D, Lungu OI, Jaehrig A, Schlichting I, Kuhlman B, Hahn KM (2009). A genetically encoded photoactivatable Rac controls the motility of living cells. *Nature* 461, 104–108.
- Xia P, Zhou J, Song X, Wu B, Liu X, Li D, Zhang S, Wang Z, Yu H, Ward T, et al. (2014). Aurora A orchestrates entosis by regulating a dynamic MCAK-TIP150 interaction. *J Mol Cell Biol* 6, 240–254.
- Zhang X, Ems-Mcclung SC, Walczak CE (2008). Aurora A phosphorylates MCAK to control ran-dependent spindle bipolarity. *Mol Biol Cell* 19, 2752–2765.
- Zong H, Hazelbaker M, Moe C, Ems-Mcclung SC, Hu K, Walczak CE (2021). Spatial regulation of MCAK promotes cell polarization and focal adhesion turnover to drive robust cell migration. *Mol Biol Cell* 32, 590–604.